

Discovery of photon index saturation in the black hole binary GRS 1915+105

Lev Titarchuk¹ and Elena Seifina²

ABSTRACT

We present a study of the correlations between spectral, timing properties and mass accretion rate observed in X-rays from the Galactic Black Hole (BH) binary GRS 1915+105 during the transition between hard and soft states. We analyze all transition episodes from this source observed with Rossi X-ray Timing Explorer (*RXTE*), coordinated with Ryle Radio Telescope (RT) observations. We show that broad-band energy spectra of GRS 1915+105 during all these spectral states can be adequately presented by two Bulk Motion Comptonization (BMC) components: a hard component (BMC1, photon index $\Gamma_1 = 1.7 - 3.0$) with turnover at high energies and soft thermal component (BMC2, $\Gamma_2 = 2.7 - 4.2$) with characteristic color temperature ≤ 1 keV, and the redskewed iron line (LAOR) component. We also present observable correlations between the index and the normalization of the disk “seed” component. The use of “seed” disk normalization, which is presumably proportional to mass accretion rate in the disk, is crucial to establish the index saturation effect during the transition to the soft state. We discovered the photon index saturation of the soft and hard spectral components at values of $\lesssim 4.2$ and 3 respectively. We present a physical model which explains the index-seed photon normalization correlations. We argue that the index saturation effect of the hard component (BMC1) is due to the soft photon Comptonization in the converging inflow close to BH and that of soft component is due to matter accumulation in the transition layer when mass accretion rate increases. Furthermore we demonstrate a strong correlation between equivalent width of the iron line and radio flux in GRS 1915+105. In addition to our spectral model components we also find a strong feature of “blackbody-like” bump which color temperature

¹Dipartimento di Fisica, Università di Ferrara, Via Saragat 1, I-44100 Ferrara, Italy, email:titarchuk@fe.infn.it; ICRANET Piazzale d. Repubblica 10-12 65122 Pescara, Italy; George Mason University Fairfax, VA 22030; and US Naval Research Laboratory, Code 7655, Washington, DC 20375; email:Lev.Titarchuk@nrl.navy.mil; Goddard Space Flight Center, NASA, code 663, Greenbelt MD 20771, USA

²Moscow State University/Sternberg Astronomical Institute, Universitetsky Prospect 13, Moscow, 119992, Russia; seif@sai.msu.ru

is about 4.5 keV in eight observations of the intermediate and soft states. We discuss a possible origin of this “blackbody-like” emission.

Subject headings: accretion, accretion disks—black hole physics—stars:individual (GRS 1915+105):radiation mechanisms: non-thermal—physical data and processes

1. Introduction

The study of the characteristic changes in spectral and variability properties of X-ray binaries is proved to be a valuable source of information on the physics governing the accretion processes and on the fundamental parameters of black holes (BHs).

The simultaneous study of the spectral and timing evolution of a BH source during a state transition has been a subject of many investigations [see references in a review by Remillard & McClintock (2006)]. Fender & Belloni (2004), hereafter FB04, introduced a classification of the spectral states in GRS 1915 +105 and studied the spectral state evolution. Using X-ray colors (hardness ratio) they introduced three spectral states. State A: in which the strong blackbody-like (BB) component of color temperature $\gtrsim 1$ keV dominates in the overall spectrum and little time variability is detected. State B: similar to state A but substantial red-noise variability on scales > 1 s occurs in this state. State C: the spectra are harder than those in states A and B. Photon indices of the power-law components vary from 1.8 to 2.5. White-red noise (WRN) variability on scales > 1 s takes place in this state.

Furthermore FB04 discussed the connection between states A, B, C observed in GRS 1915 with the three “canonical” states in black hole candidates (BHCs) also identified by their timing and spectral properties.

At a low luminosity state the energy spectrum is dominated by a hard Comptonization component combined (convolved) with a weak thermal component. The spectrum of this low (luminosity) hard state (LHS) is presumably a result of Comptonization (upscattering) of soft photons, originated in a relatively weak accretion disk, off electrons of the hot ambient plasma [see e.g. Sunyaev & Titarchuk (1980)]. Variability in LHS is high (fractional root-mean-square variability is up to 40%) and presented by a flat-top broken power law (white-red noise) shape, accompanied by quasi-periodic oscillations (QPOs) in the range of 0.01-30 Hz, observed as narrow peaks in the power density spectrum (PDS). In high soft state (HSS) a photon spectrum is characterized by a prominent thermal component which is probably a signature of a strong emission coming from a geometrically thin accretion disk. A weak power-law component is also present at the level of not more than 20% of the total

source flux. In the HSS the flat-top variability ceases, QPOs disappear and PDS acquires a pure power-law shape. The total variability in HSS is usually about 5% fractional rms. The intermediate state (IS) is a transitional state between LHS and HSS. Note in addition to LHS, IS and HSS sometimes very soft state (VSS) is observed in which the BB component is dominant and the power-law component is either very weak or absent at all. The bolometric luminosity in VSS is a factor of 2-3 lower than that in HSS.

FB04 concluded that probably all three states A, B, C of GRS 1915+105 are instances of something similar to the HSS/IS observed in other BHC systems, associated to the high accretion rate value for this source, although during the hardest intervals LHS might be sometimes reached. We come to the similar conclusions analyzing spectral and timing data from GRS 1915+105 obtained by *RXTE* (see below).

Close correlations of nearly periodic variability [quasi-periodic oscillations (QPO)] observed during low-hard and intermediate states with the photon index of the Comptonization spectral component have been reported in multiple state transitions observed from accreting BHs [see Vignarca et al. (2003), Shaposhnikov & Titarchuk (2006), (2007), (2009), hereafter V03, ST06, ST07 ST09 respectively]. The ubiquitous nature of these correlations suggests that the underlying physical processes which lead to the observed variability properties are closely tied to the corona; furthermore, they vary in a well defined manner as the source makes a transition between spectral states. The fact that the same correlations are seen in many sources, which vary widely in both luminosity (presumably with mass accretion rate) and state, suggests that the physical conditions controlling the index and the low frequency QPOs are characteristics of these sources. Moreover, they may be an universal property of all accreting compact systems, including neutron sources too [see Titarchuk, & Fiorito (2004), hereafter TF04, and Titarchuk & Shaposhnikov (2005)].

When a BH is in LHS, radio emission is also detected and a jet is either seen or inferred (Fender et al. 2001). Several models are successful in reproducing the energy spectrum from the radio domain to the hard X-rays [see e.g. Markoff et al. (2001), Vadawale et al. (2001), Corbel & Fender (2002), Markoff et al. (2003) and Giannios (2005)]. The multiplicity of models that can fit well the time average spectrum of galactic BHs indicates that this alone is not enough to distinguish the most realistic one among them. X-ray timing features can be the key features to finally finding the common physical connection between the corona, the accretion disk and the jet radio emission in BHs.

There is a big debate in the literature on the origin of quasiperiodic oscillation (QPO) frequencies [see e.g. Remillard & McClintock (2006)] and its connection with the radio emission. Migliari et al. (2005) reported on correlation between radio luminosity and X-ray timing features in X-ray binaries containing a number of low magnetic field neutron stars and

one black hole GX 339-4. They showed that in the low-hard state (LHS) radio luminosity is correlated with the low frequency QPO (LFQPO). Note ST09 demonstrate that in LHS of Galactic BHs LFQPO changes by order of magnitude, from 0.2 to 2 Hz whereas the photon index has almost the same value of 1.5. Below we show that in GRS 1915+105 the photon index monotonically increases with LFQPO and disk mass accretion rate, although the radio luminosity does not correlate with LFQPO and X-ray luminosity in the whole range of spectral states, from low-hard to high-soft through intermediate states. Recently Kylafis et al. (2008) suggested a model which explains how the QPO phenomenon is related to an appearance of radio flares (jets). Below (see §3) we present details of our observational study of the QPO connection with the X-ray and radio flaring activity in GRS 1915+105.

In LHS and IS which we consider in our study, only a small part of the disk emission component is seen directly. The energy spectrum is dominated by a Comptonization component presented by a power law. To calculate the total normalization of the “seed” disk blackbody component we model the spectrum with a Generic Comptonization model [BMC XSPEC model, see details in Titarchuk, Mastichiadis & Kylafis (1997)] which consistently convolves a disk blackbody with a Green function of the Compton Corona to produce the Comptonization component. We argue that the disk emission normalization calculated using this approach produces a more accurate correlation with respect to the correlation with the direct disk component which was obtained using the additive model, multicolor disk plus power law [see e.g. McClintock & Remillard (2006)].

This Paper is a continuation of the study of index-QPO and index-seed photon normalization correlations in BH sources started in ST07 and ST09. Particularly here we present a study of the index-seed photon normalization (disk flux) correlation observed from GRS 1915+105 when it evolves from LHS to HSS. The description of *RXTE* data-set used is given in §2. We have analyzed a broader sample of state transitions from GRS 1915+105 and we found a diverse phenomenology for index evolution through a transition. In §3 we provide a detailed description of state transitions analyzed in this study. In §4 we discuss and interpret the results of our observational study. Specifically in §4 we consider the effect of the bulk motion Comptonization in the inner part of the accretion flow on the index evolution during a state transition. Also we show that the index saturation effect is a direct consequence of the existence of this inner bulk motion region and, therefore, can be considered as an observational signature of the converging flow (black hole). Furthermore in §4 we discuss the TF04 model and the Monte Carlo simulations by Laurent & Titarchuk (2009) (in preparation) in which the observable index evolution with \dot{m} has been already predicted. Conclusions follow in §5.

2. Observations and Data Reduction

In the present Paper, we have used publicly available data of the *RXTE* observatory obtained from January 1997 to April 2006. In total, our study includes 107 observations made at different BH spectral states (LHS, IS, HSS) of the system. Data sets were selected to represent a complete rise-middle-decay track of bright X-ray activity episodes behavior along bright radio flaring events ($S_{15GHz} \geq 250$ mJy). Therefore we have chosen powerful (≥ 250 ASM counts/s) flaring episodes of GRS 1915+105 with a good coverage of simultaneous radio/X-ray observation. In the past some of these data of spectral transitions in GRS 1915+105 were analyzed by Trudolyubov et al. (1999), Trudolyubov (2001), Munro et al. (1999), Reig et al. (2000), ST07 and Rodriguez et al. (2008) for the 1997 – 1998 and 2005 – 2006 transitions respectively.

Standard tasks of the LHEASOFT/FTOOLS 5.3 software package were utilized for data processing using methods recommended by RXTE Guest observer Facility according to “The RXTE Cook Book” (http://heasarc.gsfc.nasa.gov/docs/xte/recipes/cook_book.html). For spectral analysis we used PCA *Standard 2* mode data, collected in 3 – 20 keV energy range. The standard dead time correction procedure has been applied to the data. To construct broad-band spectra, data from HEXTE detectors have also been used. We subtracted background corrected in off-source observations. Only HEXTE data in 20 – 150 keV energy range were used for the spectral analysis in order to exclude the channels with largest uncertainties. The HEXTE data have been re-normalized based on the PCA. The data are available through the GSFC public archive (<http://heasarc.gsfc.nasa.gov>). In Tables 1-6 we list groups of observations covering the complete dynamical range LHS-(IS)-HSS-(IS)-LHS of the source evolution during flaring events. We present here period ranges MJD=50462 – 51081 and MJD=53382 – 53852, as different types (samples) of bright X-ray activity, with transitions between hard and soft states. Two selected data sets have different patterns of radio/X-ray behavior and of light curve shapes.

We also use public GRS 1915+105 data from the All-Sky Monitor (ASM) on-board *RXTE* (Swank 1999). The ASM light curves (2-12 keV energy range) were retrieved from the public *RXTE*/ASM archive at HEASARC (http://xte.mit.edu/ASM_lc.html).

The monitoring *Ryle Radio Telescope* (15 GHz) data in the 1997 – 2006 period were kindly provided by Dr. Guy Pooley. The technical details of the radio telescope are described by Pooley & Fender (1997).

2.1. Spectral analysis

2.1.1. BMC and iron line components of the model spectrum

The broad-band source spectra were modeled in XSPEC with an additive model consisting of *two BMC*: a BMC with high energy cut-off (*BMC1* component) and *BMC2* component: $wabs * (bmc + bmc * highecut)$. We also use a multiplicative *wabs* model to take into account of an absorption by neutral material. The *wabs* model parameter is an equivalent hydrogen column N_H . Systematic error of 1% has been applied to the analyzed X-ray spectra.

The *BMC* model describes the outgoing spectrum as a convolution of the input “seed” blackbody-like spectrum, whose normalization is N_{bmc} and color temperature is kT , with the Comptonization Green’s function. Similarly to the ordinary *bbody* XSPEC model, the normalization N_{bmc} is a ratio of the source (disk) luminosity to the square of the distance

$$N_{bmc} = \left(\frac{L}{10^{39} \text{erg/s}} \right) \left(\frac{10 \text{ kpc}}{d} \right)^2. \quad (1)$$

The resulting spectrum is characterized by the parameter $\log(A)$ related to the Comptonized fraction f as $f = A/(1 + A)$ and a spectral index $\alpha = \Gamma - 1$. There are several advantages of using the BMC model with respect to other common approaches used in studies of X-ray spectra of accreting compact objects, i.e. sum of blackbody/multi-color-disk and power-law/thermal Comptonization. First, the BMC, by the nature of the model, is applicable to the general case where there is an energy gain through not only thermal Comptonization but also via dynamic (bulk) motion Comptonization (see Shaposhnikov & Titarchuk 2006, for details). Second, with respect to the phenomenological *powerlaw* model, the BMC spectral shape has an appropriate low energy curvature, which is essential for a correct representation of the lower energy part of spectrum. Our experience with *powerlaw* components shows that the model fit with this component is often inconsistent with the N_H column values and produces an unphysical component “conspiracy” with the *highcut* part. Specifically, when a multiplicative component *highcut* is combined with BMC, the cutoff energies E_{cut} are in the expected range of 20~30 keV, while in a combination with *powerlaw*, E_{cut} often goes below 10 keV, resulting in unreasonably low values for photon index. As a result, the implementation of the phenomenological *powerlaw* model makes much harder, or even impossible to correctly identify the spectral state of the source, which is an imminent task for our study. Third, and even a more important property of the BMC model, it calculates consistently the normalization of the original “seed” component, which is expected to be a correct mass accretion rate indicator. Note the Comptonized fraction is properly evaluated by the BMC model.

We consider a scenario related to our spectral model (see Fig. 1) where the Compton

cloud along with converging flow are located in the innermost part of the source and the Keplerian disk is extended from the Compton cloud (CC) to the optical companion (see e.g. TF04). An iron K_α -line (*laor*) component (Laor 1991) was included in our model spectrum. To summarize the spectral model parameters are the equivalent hydrogen absorption column density N_H ; spectral indices α_1, α_2 (photon index $\Gamma = \alpha + 1$); color temperatures of the blackbody-like photon spectra kT_1, kT_2 ; $\log(A_1), \log(A_2)$ related to the Comptonized fractions f_1, f_2 [$f = A/(1 + A)$]; normalizations of the blackbody-like components N_{bmc1}, N_{bmc2} for the *BMC1* and *BMC2* components of the resulting spectrum, respectively.

We find that color temperatures kT_1 and kT_2 are about 1 keV for all available data and thus we fix values of kT_1 and kT_2 at 1 keV. An equivalent hydrogen absorption column density was fixed at the level of $N_H = 5 \times 10^{22} \text{ cm}^{-2}$ (Trudolyubov 2001). When the parameter $\log(A) \gg 1$ we fix $\log(A) = 2$ (see Tables 1-6), because the Comptonized fraction $f = A/(1 + A) \rightarrow 1$ and variation of A does not improve the fit quality any more.

During LHS the BMC2 component is often very low or barely detectable [see Table 1 (MJD=50462-50561), Table 3 (MJD=51067-51081), Table 6 (MJD=53829-53852) and Fig. 2 and panel “1S”]. This observational fact is in agreement with scenario of BH spectral state transition (TF04). During LHS the spectrum is characterized by a strong hard power-law component. In other words the energy spectrum is dominated by a Comptonized component seen as a power-law hard emission in energy range from ~ 10 to ~ 70 keV while the disk emission remains weak (LHS, IS), because only a small fraction of the disk emission component ($1 - f$) is directly seen (Fig. 2, panel “1S”).

Although during IS (Fig. 2, panel “2S”) the contributions of two BMC components to the overall spectrum are of the same order sometimes we can barely identify one of these components [see these cases in Table 2, (MJD=50737, 50743), Table 3 (MJD=50908, 50909, 51003), Table 5 (MJD=53718) when $N_{bmc2} \ll N_{bmc1}$]. On the other hand the model with two BMC components are really needed in the most cases of the intermediate state (IS) and high-soft state (HSS). In Figure 3 we demonstrate that the fit qualities are unacceptable when the only one BMC component is included in the spectrum. Specifically, for IS-HSS observation 91701-01-11-00 on 18 May 2005 the values of $\chi_{red}^2=12.3$ for 75 d.o.f. (bottom left panel) for *wabs*bmc*highcut* model. However χ^2 is significantly improved when the second BMC component is included in the model. For *wabs*(bmc + bmc*highcut)* $\chi_{red}^2=3.28$ for 76 d.o.f. (see the related count spectrum along with the model and the related residual in the central bottom panel of Fig. 3). Ultimately we achieve a remarkable agreement with the data using *wabs*(bmc + bmc*highcut + laor)* model for which $\chi_{red}^2=1.04$ for 73 d.o.f. In Figure 3 (top and right bottom panels) we show the data along with the best-fit spectra and their components for our two component BMC model (see Table 4 for the best-fit parameter

values).

In HSS and very soft state (VSS) (MJD=53515-53640, Table 4) the soft luminosity is high and the spectrum is dominated by a thermal component ($\Gamma_2 > 3.7$). Note the hard power-law component is barely seen in VSS (see Fig. 2, panels “4S”). We find a broad emission line between 6 and 7 keV in the IS and HSS spectra. Up to the date the iron K_α emission line in IS and HSS of GRS 1915+105 was detected with ASCA, Chandra, XMM-Newton, BeppoSAX by Kotani et al. (2000), Martocchia et al. (2002), Miller & Homan (2005). However the determination of the iron line shape with *RXTE* is a problem because of the low energy resolution. As a first trial we added a Gaussian component to fit the spectrum varying the width and normalization of the line. Fits using the Gaussian always produce residuals around 7 keV while fits with XSPEC Laor model do not have such a problem. Thus through the Paper we incorporate the Laor-line profile to fit the line component. The line feature has a statistical significance of (3-10) σ depending on the spectral states. This line feature is variable with time average intensity of 2×10^{-11} erg/s/cm² and exhibits equivalent width (EW) in the range of 50-600 eV across the data. We found that adding the laor-line component significantly improves the fit quality of IS and HSS spectra. Fitting an IS spectrum (e.g. for 90105-05-03-05 observation) without the line components leads to $\chi_{red}^2=1.24$. When the line component (Laor) is included the fit quality becomes much better, $\chi_{red}^2=1.01$. The fit of HSS spectrum (901050-08-02-00) without the iron-line component is unacceptable, $\chi_{red}^2=2.01$, and $\chi_{red}^2=1.24$ when the line component is included. The best-fit parameters of the source spectrum and values of χ_{red}^2 including d.o.f are presented in Tables 1-6.

2.1.2. Observational evidence of “blackbody-like” component peaked at ~ 20 keV in eight IS spectra

The adopted spectral model shows a very good performance for 99 cases among 107 spectra used in our analysis. Namely, the value of reduced χ^2 -statistic $\chi_{red}^2 = \chi^2/N_{dof}$, where N_{dof} is a number of degree of freedom for a fit, is less or around 1.0 for most observations. However for 8 observations of intermediate state the fit of the data with the model *wabs*(bmc*highcut+bmc+laor)* is not so good, χ_{red}^2 reaches 1.5 and even higher. We found that in the residual of data vs model there is a characteristic bump around 20 keV (see left bottom panel of Fig. 4) which can be fitted by blackbody-like shape of color temperature about 4.5 keV (see right bottom and top panels of Fig. 4 and Table 7 for values of the best-fit parameters). This “high-temperature BB” component is strong in each of the eight observations and its EW varies from 400 to 700 eV. We discuss a possible origin of this “BB”

component in §4.

2.2. Timing analysis

The *RXTE* light curves were analyzed using the *powspec* task. For the timing analysis in 2 – 30 keV energy range, we use the *RXTE*/PCA data in the *binned* and *event* modes containing X-ray events below 13/15 keV and above 13/15 keV for 1997/2005 data sets respectively. Specifically, depending on *RXTE* epoch, the channel ranges (0-35) for binned and (36-255) for event modes relate to energy bands 1.94-12.99 keV (binned) and 13.36-103.19 keV (event) for epoch 3 (1997-1998 data set), and relate to 2.06-14.76 keV (binned) and 15.18-117.86 keV (event) for epoch 5 (2005-2006 data set).

The time resolutions for event and binned modes are 1.52×10^{-5} s and 8×10^{-3} s, respectively. The observational exposition time periods vary from 1.5 to 10 ks. Thus for all of these observations we can obtain power spectra in the wide frequency range (roughly from 0.001 Hz up to 100/10000 Hz for binned and event modes respectively). These frequency ranges allow us to produce power spectra for all studied cases in the 0.1-100 Hz frequency range. We subtracted the contribution due to Poissonian statistics and Very Large Event Window for all power density spectra (PDS).

The data analysis of the PDSs was performed using a simplified version of the diffusion model [see Titarchuk, Shaposhnikov & Arefiev (2007), hereafter TSA07, and Titarchuk & Shaposhnikov (2008)] in which the PDS continuum shape at frequencies below the driving frequency can be approximated by empirical model $P_X \sim (1.0 + (x/x_*)^2)^{-in}$ (*KING* model in QPD/PLT). Following TSA07, the break frequency found in the PDS is related to a diffusion time of perturbation propagation while the QPO low frequency is an eigenfrequency of the volume (magnetoacoustic) oscillation of the medium (in our case it is a Compton cloud). Note, TSA07 demonstrated that the diffusion model as a linear superposition of Lorentzians related to the eigenvalues of the diffusion problem can be also presented by the continuous shape which is flat below break frequency and power law at frequencies above the break. Given these asymptotic forms of PDS at low and high frequency limits they named their diffusion model as a white-red noise (WRN) model. For the quasi-uniform perturbation source distribution the slope of the PDS power-law part depends on the law of viscosity in the corona or in the disk (see details in TSA07). The parameters of this WRN diffusion model are the break (diffusion) frequency and the index of the power-law distribution of the viscosity over the radius. To fit the QPO features, we use Lorentzian shape. We quote the Lorentzian centroid as a QPO frequency.

3. Observational results

3.1. Evolution of spectral properties during state transitions

Observations of Galactic BH X-ray binaries reveal diverse spectral and dynamic phenomenologies. The evolution of a BH binary is usually described in terms of spectral states. There are several flavors of BH state definitions in literature, which slightly differ in BH state definitions and terminology (see, for example Remillard & McClintock 2006; Belloni et al. 2000, 2005; Klein-Wolt & van der Klis 2008). To distinguish different states, the properties observed in the energy spectrum and Fourier power density spectrum (PDS) are utilized. As we have already emphasized in the introduction section we use, in our study, the general state classification for four major BH states: *low-hard* (LHS), *intermediate* (IS), *high-soft* (HSS) and *very soft* state (VSS).

The general picture of LHS-IS-HSS transition is illustrated in Figure 5 where we bring together spectra of LHS, IS, HSS and VSS to demonstrate the source spectral evolution from low-hard to soft states. We should emphasize different shapes of the spectra for the different spectral states. In the LHS spectrum the Comptonization component is dominant and the blackbody (BB) component is barely seen in 3-150 keV energy range. The IS and HSS spectra are characterized by a strong soft BB component and a power law extended up to 150 keV. In VSS the soft BB component is dominant and the power-law component is relatively weak with respect of this in IS and HSS.

In the RXTE data of GRS 1915+105 observations there are long periods when the photon index Γ_1 and normalization N_{bmc1} of the hard BMC monotonically increase (or decrease) with time. We call these periods as long transition periods. The days, when the source X-ray flux starts to increase while it is still in the LHS, can be considered as a beginning of the rise transition. In these times the energy spectrum is characterized by low index values $\Gamma_1 \sim 1.7$ and the thermal component is at low level or undetectable at all. In Figure 6 from top to bottom we show an evolution of flux density S_{15GHz} at 15 GHz (Ryle Telescope), *RXTE*/ASM count rate, BMC normalization and photon index Γ during the 1997 rise transition of GRS 1915+105 (MJD 50500 – 50700). Red/black points (*for two low panels*) correspond to hard/soft components with Γ_1 and Γ_2 , respectively. In the bottom we plot the photon index Γ versus the BMC normalization (*left*) and Comptonized fraction (*right*) for this transition. Here red triangles/black circles correspond to hard/soft components with Γ_1 and Γ_2 , correspondingly. One can see that in the beginning of this transition the resulting spectrum consists of one Comptonization component whose photon index Γ_1 steadily increases *from 1.7* towards the softer states and finally saturates at the value of 3. The Comptonization fraction $f = A/(1 + A)$ of the hard component, related to index Γ_1 , shows

a sign of decreasing towards the softer state. When the *RXTE*/ASM count rate exceeds 50 counts/s the soft Comptonized component appears with a weight which is comparable to that of the hard component. The photon index of the soft component Γ_2 saturates to the level of 4.2 when the BMC normalization (disk flux) increases. The Comptonization fraction f of the soft component is about 0.5 and higher.

As seen from Fig. 6 the start of this rise transition coincides with active phase of X-rays, and of radio emissions which exceed 10 ASM counts/s and 50 mJy levels respectively in the 1997 rise transition. Around MJD 50580 day the source reaches the HSS (when $\Gamma_1 \sim 3$). Then a long HSS period from MJD 50580 to 50700, when Γ_1 stays almost the same, is followed by the state transition to IS during which Γ_1 decreases to 2.5 (see Fig. 7-8).

We see a similar behavior of X-ray, radio fluxes and photon indices during the 2005 bright X-ray episode. The only difference of that with the 1997 episode was that the 2005 rise started at the intermediate state and went very quickly to HSS (see Fig. 9-10). After MJD 53800 the source came back to IS-LHS when $\Gamma_1 \lesssim 2$ (see Fig. 10 and Table 6). Note typical X-ray and radio fluxes during IS are about 40-60 ASM counts/s and ≤ 50 mJy respectively.

3.2. Observational (correlated and non-correlated) characteristics of X-ray and radio emissions

In fact, we do not find any correlation of X-ray and radio fluxes when the source changes its spectral states. Also we do not find a correlation of radio activity with the X-ray photon index (see Fig. 11). However we find a strong correlation of the iron line EW with radio flux density $S_{15\text{GHz}}$ at 15 GHz (see Fig. 12). In Figure 12 we also include points which have been recently reported by Neilsen & Lee (2009) who have analyzed archival HETGS (High Energy Transmission Grating Spectrometer) observations of GRS 1915+105 from the Chandra X-ray Observatory.

The prominent HSS events were observed during 2005 – 2006 observations around MJD 53490 and MJD 53690 (see Figs. 9-10). The 2005 – 2006 observations confirm the index evolution vs BMC normalization (disk flux) found in the 1997 – 1998. The indices of the hard and soft components indeed increase and then saturate at values of $\lesssim 3$ and 4.2 respectively (see Fig. 10). Index Γ_1 started a saturation at lower values of BMC1 normalization (presumably proportional to disk mass accretion rates) than that were in 1997.

It is also worth noting a so called “pivoting” effect, i.e. when inequality $N_{bmc1} > N_{bmc2}$ switches to $N_{bmc2} > N_{bmc1}$ or vice versa, which is seen in the 1997-1998 and 2005 - 2006 observations. One can see this composite pivoting picture combining Figs. 6-10. In fact,

these pivoting points correspond to the spectral transitions between adjacent states LHS-IS to HSS and vice versa.

In Figure 13 we collect all data points for the index-normalization correlation for rise and decay stages. We do not find much differences in the correlation patterns related to the rise and decay transitions (compare left and right panels) in contrast that ST09 found in other BHs.

We also find that the photon index of X-ray spectrum is tightly correlated with the quasi-periodic oscillations (QPO) frequency (see Fig. 14) which can be considered as a strong argument that QPOs and X-ray Comptonization spectrum emerge from the same geometrical configuration (Compton cloud). However the flux density S_{15GHz} and QPO frequency are not correlated with each other when the source changes its spectral states. In Figure 15 we show an evolution of the flux density S_{15GHz} at 15 GHz (Ryle Telescope), *RXTE*/ASM count rate and ν_{QPO} during 1997 (left column) and 2005 (right column) rise transitions. The left column panel demonstrates the presence of QPO during a low radio activity (<30 mJy). The right column panel shows an example of the presence of QPO when the radio flux is high ($\sim 100 - 200$ mJy). Given that the quasi-periodic oscillations (QPOs) of X-ray flux are present independently of the radio flux level, we can conclude that the radio appearances and QPO phenomenon are not closely related and probably the radio and X-ray (oscillating) emission areas have different origins in the source.

3.3. Evolutions of energy and power spectra during a minor X-ray/radio flares

In Figure 16 we show the details of a typical evolution of X-ray timing and spectral characteristics for minor X-ray/radio flares. In the top panels of Figure 16 we show the flux density S_{15GHz} at 15 GHz (Ryle Telescope) and the *RXTE*/ASM count rate during the 2005 rise transition stage (see also Fig. 9). Red points A, B and C on the panel of the *RXTE*/ASM count rate vs time correspond to moments at MJD=53416, 53422 and 53442 (before, during and after the minor X-ray/radio flare) respectively. Points A and C were chosen as the nearest possible points to point B (taking into account the time-table of archive data). Point B corresponds to the maximum of radio flux of 300 mJy and EW of 600 eV. Note that QPO centroid frequency before the flare (at point A) is at 1.8 Hz and shifts to 0.9 Hz (point C) after the flare.

PDSs (left bottom column) are plotted versus the energy spectrum (right bottom column) for three points A (top), B (middle) and C (bottom) of the X-ray light curve. There

are QPOs at A and C points (A1, C1 panels) but there is none at B point (B1 panel), at the X-ray flare peak. For the photon spectra (right bottom column) red points stand for observational data, while the model is shown by components with blue line for *BMC1*, black line for *BMC2* and dashed purple line for the *laor* line component. Note that the spectral characteristics undergo noticeable changes during X-ray/radio flare. Specifically at the flare peak (point B) the total flux increases at least by a factor of 1.5 with respect to that before the flare. Although photon index of *BMC1* component Γ_1 changes from 2.9 (A and C points) to 3.0 (B point) respectively.

We also studied the energy dependence of the PDS shape and integrated power variability as a function of the photon energy. In Fig. 16 (*left bottom column pannel*) we show two power spectra for two energy bands 2-15 keV (red) and 15-30 keV (blue). One can see that PDSs weakly depend on the energy band. In particular, a value of the low frequency QPO ν_{QPO} is the same for the low energy and high energy PDSs.

4. Interpretation and discussion of observational results

Before to proceed with the interpretation of the observations let us to briefly summarize them as follows: i. The spectral data of GRS 1915+105 are well fit by two (soft and hard) BMC components for most of analyzed IS and HSS spectra (see Fig. 3) while LHS spectra essentially require only one BMC component, the soft BMC component is very weak (see Tables 1, 3-4, 6 and panel S1 in Fig. 2). ii. In addition to two BMC components 8 IS-HSS spectra require an extra component which can be fitted by “high temperature BB-like” profile (see Fig. 4 and Table 7). iii. The Green’s function indices of each of these components rise and saturate with an increase of the BMC normalization (disk flux). The photon index saturation levels of the soft and hard components are about 4.2 and 3 respectively (see Fig. 13). iv. We also find a tight positive correlation of QPO frequencies with the index (see Fig. 14) and consequently that with the disk flux. vi. The iron line EW correlates with the radio flux (see Fig. 12). vii. QPO appearances and their frequency values are not correlated with radio flux when the source undergoes the spectral changes from IS to HSS (see Fig. 15). viii. We also do not find any correlation between X-ray and radio fluxes and X-ray power-law index (see Fig. 11). ix. Although we find changes of power and energy spectra during a minor X-ray/radio flares when QPO features disappear in PDS and energy spectrum becomes softer than that was before and after the flare (see Fig. 16).

4.1. Index-QPO and index- \dot{m} correlations. Index saturation

We confirm the index-QPO correlation in GRS 1915+105 previously found by V03 and ST07. This correlation was indeed predicted by Titarchuk, Lapidus & Muslimov (1998), hereafter TLM98, who argued that the transition layer [Compton cloud (CC)] formed between the Keplerian disk and the central object (NS or BH), contracts and becomes cooler when the disk mass accretion rate \dot{m} increases. The observational effect of the CC contraction were later demonstrated by ST06, TSA07, TS08 and Montanari, Titarchuk & Frontera (2009) in Cyg X-1 and XTE J1650-500 respectively. As a result of the transition layer (TL) contraction the QPO low frequency ν_L , which is presumably the TL's normal mode oscillation frequency, increases with \dot{m} given that ν_L is inversely proportional to the TL size. On the other hand the index monotonically increases when the TL (CC) cools down. TF04 provided the details of the index-QPO correlation model where they pointed out that this correlation is a natural consequence of the spectral state transition.

In this Paper we have firmly established the index correlation with ν_L along with the index saturation vs the BMC normalization N_{bmc} (Eq. 1) for the soft and hard Comptonized components of the X-ray spectra of GRS 1915+105 (see Fig. 13). Below we show that N_{bmc} is actually proportional to mass accretion rate in the disk. Namely the disk flux L (as a source of soft photons for Comptonization, see e.g. Fig. 1 for the geometry of soft photon illumination of Comptonized region) can be represented as

$$L = \frac{GM_{bh}\dot{M}}{R_*} = \eta(r_*)\dot{m}_d L_{Ed}. \quad (2)$$

Here $R_* = r_* R_S$ is an effective radius where the main energy release takes place in the disk, $R_S = 2GM/c^2$ is the Schwarzschild radius, $\eta = 1/(2r_*)$, $\dot{m}_d = \dot{M}_d/\dot{M}_{crit}$ is dimensionless mass accretion rate in units of the critical mass accretion rate $\dot{M}_{crit} = L_{Ed}/c^2$ and L_{Ed} is the Eddington luminosity.

On the other hand

$$L_{Ed} = \frac{4\pi GMm_p c}{\sigma_T} \quad (3)$$

i.e. $L_{Ed} \propto M$ and thus using Eqs. (2-3) we obtain that

$$L \propto \eta(r_*)\dot{m}_d m. \quad (4)$$

In HSS when the inner disk radius R_* reaches its lowest value $R_* \gtrsim 3R_S$, the efficiency of the gravitational energy release $\eta(r_*)$ reaches its highest value and thus the disk flux increases only when the disk mass accretion rate increases (see Eq. 4). Given that BMC normalization

N_{bmc} is proportional to \dot{m}_d in HSS the observational effect of the index saturation with N_{bmc} is translated to the index saturation with \dot{m}_d .

First we interpret the index saturation related to the hard Comptonization component (*BMC1*). We suggest that this BMC1 component of the emergent spectrum is presumably originated in the converging flow onto a compact object, in our case to the BH (see Fig. 1). In fact, in HSS the plasma temperature of the accretion flow is comparable with the color temperature of the disk photons (see TF04). Thus, in order to explain the high energy tail observed in HSS of BH sources, one should assume either an unknown source of high energy non-thermal electrons [see e.g. Coppi (1999)] or consider effects of energy transfer from the converging flow electrons to the photons emitted from the innermost part of the accretion flow.

Optical depth of the converging flow τ is proportional to \dot{m}_d if one assumes that disk accretion flow continuously goes to the converging flow and there are no other components in the accretion flow [see e.g. a model of two component accretion flow by Chakrabarti & Titarchuk (1995), hereafter CT95]. This effect of the index saturation vs optical depth of the bulk flow (BM) τ was first predicted by Titarchuk & Zannias (1998) and then it was subsequently reproduced in Monte-Carlo simulations by Laurent & Titarchuk (1999), hereafter LT99.

It is worth noting that the index saturation effect is an intrinsic property of the bulk motion onto a BH given that the spectral index $\alpha = \Gamma - 1$ is a reciprocal of the Comptonization parameter Y [see this proof in ST09 and Bradshaw et al. (2007)] which saturates when the BM optical depth, or \dot{M} , increases. In fact, the Y -parameter is a product of the average photon energy exchange per scattering η and the mean number of photon scattering N_{sc} , i.e. $Y = \eta N_{sc}$. For the thermal Comptonization case, $Y \sim (4kT/m_e c^2)\tau^2$ given that in this case $\eta = 4kT/m_e c^2$ and $N_{sc} \sim \tau^2$ for $\tau \gg 1$ (see e.g. Rybicki & Lightman 1979) and, thus, the thermal Comptonization spectral index is

$$\alpha \sim [(4kT/m_e c^2)\tau^2]^{-1}. \quad (5)$$

In the case of converging flow, the preferable direction for upscattered photons is the direction of bulk motion onto the BH, i.e along the radius. Note that the fractional photon energy change is

$$\Delta E/E = (1 - \mu_1 V_R/c)/(1 - \mu_2 V_R/c).$$

where μ_1 and μ_2 are the cosines of the angles between the direction of the electron velocity $\mathbf{n} = \mathbf{V}_R/V_R$ and direction of incoming and outgoing (scattered) photons respectively.

The number of scatterings of the up-Comptonized photons N_{sc} can be estimated as a ratio of the radial characteristic size of the converging flow L and the free path l in the

direction of motion, namely $N_{sc} \propto L/l = \tau$ given that $\Delta E/E$ has a maximum at $\mu_2 = 1$ for given μ_1 and V_R . On the other hand the efficiency per scattering for bulk motion flow $\eta \propto 1/\tau$ when $\tau \gg 1$ [Laurent & Titarchuk (2007), hereafter LT07] hence for bulk motion Comptonization, the Y-parameter does not depend on τ for high values of τ or dimensionless mass accretion rate \dot{m} . Thus one can conclude that *the Comptonization parameter $Y = \eta N_{sc}$ and hence the energy index $\alpha = Y^{-1}$ saturate to a constant value when optical depth (or mass accretion rate) of the BM flow increases.*

However the index saturation value is determined by the plasma temperature during a transition [see LT99]. The plasma temperature strongly depends on the mass accretion rate in the bulk motion region \dot{M}_{bm} and its illumination by the disk photons L (see TLM98 and TF04). For higher \dot{M}_{bm} and L the plasma temperature is lower. The level of the index saturation decreases when the plasma temperature in the bulk motion increases (TF04). Thus the index saturation levels can be different from source to source depending on the strength of the disk. Looking at Figure 13 one can also notice that the index Γ_1 starts its saturation at different values of BMC normalization ($\propto \dot{m}_d$) for different types of active episodes. In fact, the index should saturate with mass accretion rate in the converging flow \dot{m}_{bm} which is a sum of the disk mass accretion rate \dot{m}_d and that in sub-Keplerian flow (CT95). Hence one can argue that this lower value of \dot{m}_d at which the index saturates can be a sign of the presence of extra (sub-Keplerian) component in the accretion flow onto BH in GRS 1915+105.

Laurent & Titarchuk (2009), hereafter LT09, study the index- \dot{m} correlation and also a modification of the disk blackbody spectrum due to Comptonization in the optically thick CC, which is formed due to accumulation of accretion matter in the TL. They indeed explain the saturations of the indices of the soft and hard components of the resulting spectrum. Specifically LT09 show that gravitational energy of the accretion flow is released in the optically thick and relatively cold TL when mass accretion rate \dot{m}_d is higher than 1. The level of the index saturation depends on the radial velocity in the transition layer (TL). LT09 also show that the observable saturation index of the soft BMC component $\Gamma_2 \sim 4.2$ can be reproduced in their Monte Carlo simulations for values of the TL radial velocity $\gtrsim 0.05 c$.

4.2. Physical origin of “high temperature BB-like” component”?

In 8 of IS-HSS spectra we find an observational evidence of the bump around 20 keV which can be fitted by “ ~ 4.5 keV BB-like” profile (see Fig. 4 and Table 7). One can argue that this observable bump at 20 keV is a signature of the Compton reflection bump [see e.g. Basko et al. (1974), ST80, CT95, and Magdziarz & Zdziarski (1995)]. But this

interpretation encounters difficulties given that the hard power-law tails of these spectra are too steep to form the Compton bump. Indeed, ST80 and later LT07 demonstrated that the Compton bump as a result of a photon accumulation due to downscattering of hard photons in the cold medium (for example disk) cannot be produced if the photon index of the incident hard photon spectrum $\Gamma > 2$. In fact, as one can see from Table 7, that in all spectra where we detect this ~ 20 keV feature the index of the hard BMC component $\Gamma_1 > 2$ (the indices vary between 2.5 and 3).

In principle, this bump may also be a result of photoelectric absorption of the photons below 10 keV in the cold medium (disk) even if the incident spectrum is very steep. The photoelectric absorption cross-section $\sigma_{ph} \sim (7.8 \text{ keV}/E)^3 \sigma_T$, where E is photon energy and σ_T is Thomson cross-section (e.g. CT95). However, Laming & Titarchuk (2004) and Różańska & Madej (2008) show that the ionization of such a disk by the intensive X-ray radiation during IS-HSS invalidates the basic assumptions of the presence of the cold material in the innermost part of the source. Note the hard tail of X-ray spectrum in IS-HSS is formed in the converging flow (CF), i.e. in the innermost part of the accretion flow, because we see the CF signature (the index saturation) when the source goes to IS-HSS.

On the other hand Titarchuk (2002) argued that the specific spectral and timing features of X-ray radiation could be seen in BH sources only. Particularly, he stated that the photon-photon interaction of the effectively upscattered photons results in the powerful pair production near a BH horizon. Indeed, a large fraction of the upscattered photons going inward are deflected by the relativistic free-fall electron in the outward direction [the aberration effect of light, see e.g. Rybicki & Lightman (1979) and Appendix A]. These diverted upscattered photons of energy E_{up} interact with incoming photons of energy E_{in} flux and ultimately this interaction leads to the pair creation if the condition $E_{up}E_{in} \gtrsim (m_e c^2)^2$ is satisfied. Note that free-fall bulk motion with Lorentz factor $\gamma \gg 1$ should be very close to horizon, i.e.

$$\frac{\Delta R}{R_S} \approx \frac{1}{\gamma^2} \quad (6)$$

where $\Delta R = R - R_S$ is radial distance to horizon. Thus the created positrons extensively interact with accreting electrons there and therefore the annihilation line photons are created and distributed over the relatively narrow shell near BH horizon. Specifically

$$\Delta R \lesssim 3 \times 10^4 \left(\frac{10}{\gamma} \right)^2 \frac{m}{10} \text{ cm}. \quad (7)$$

The proper energy (in the comoving flow frame) of annihilation line photons E_{511} should be seen by the Earth observer (in the zero frame) at the redshifted energy

$$E_0 = (1 - R_S/R)^{1/2} E_{511} \approx \frac{E_{511}}{\gamma} \quad (8)$$

where $(1 - R_S/R)^{1/2} \approx (\Delta R/R_S)^{1/2} = 1/\gamma$ (see according Eq. 6).

In other words the line energy displacement due to gravity as viewed by a far away observer in free space is $z + 1 = 1/(1 - R_S/R)^{1/2} = \gamma$.

A significant fraction of these annihilation line photons strongly gravitationally redshifted can be directly seen by the Earth observer as a bump located at ~ 20 keV and presumably related to the representative value of $\gamma \sim 20$. Laurent & Titarchuk (2009, in preparation) made extensive Monte Carlo simulations of the X-ray spectral formation in the converging flow taking into account photon-electron, photon-photon and pair-electron interactions. These simulations confirm our expectations that in some cases the emergent spectra of IS and HSS consists of the redshifted annihilation line located at ~ 20 keV, which can be fitted by “high temperature BB-like” profile, and also the simulated spectra are extended to energies of order of a few MeV [see Fig. 4 and Grove et al. (1998) for details of IS-HSS spectral components].

4.3. Radio–X-ray connection

Migliari et al. (2005), hereafter MFK05 reported on correlations between radio luminosity and X-ray timing (QPO) features in X-ray binary systems containing low magnetic field neutron stars and black holes. The MFK05 conclusions on the radio-QPO correlation based on observations of seven neutron star and one black hole GX 339-4. For GX 339-4 they used data only in low-hard state before and after outburst. Titarchuk & Shaposhnikov (2005) based on the analysis of *RXTE* data from NS 4U1728-34 confirmed a correlation of X-ray and radio emissions with LF QPOs through all spectral states for this particular NS source. However, we do not find a real low-hard state in GRS 1915+105 for which photon index Γ_1 should be about 1.5, as that in GX 339-4 (see ST09), and therefore we cannot confirm or refute the radio-QPO correlation in GRS 1915+105 LHS similar to that found by MFK05 in GX 339-4.

On the other hand we find that LFQPOs do not correlate with the radio flux while they correlate with the hard component photon index Γ_1 through IS and HSS (see Fig. 15 and Fig. 14 respectively). Absence of correlation between radio luminosity and QPO can be explained by the different origins of these quantities. While the QPO phenomenon is probably related to the transition layer oscillations (see §4.1), it is confirmed by the index-QPO correlation, the radio emission is presumably originated in the wind or wide open jet. Furthermore, because the radio flux and iron line EW are strongly correlated (see Fig. 12) one can conclude that the iron line is also formed in the wind [see more on the

line formation origin in LT07, Shaposhnikov, Titarchuk & Laurent (2009) and Titarchuk, Shaposhnikov & Laurent (2009)]. It is also worth noting that the X-ray flux, and photon index do not correlate with the radio flux (see Fig. 11). It can be explained by the different mechanisms of the energy releases in X-ray and radio. X-ray radiation is presumably formed in the innermost part of the disk and in the transition layer (or Compton cloud) while the radio emission is presumably formed in the jet or winds which are probably launched at the outskirts of the disk [see e.g. Meyer-Heimster & Meyer (1999), Meyer et al. (2000), Meyer-Heimster & Meyer (2003) and TSA07].

Using the aforementioned correlations of EW with radio flux we can suggest that some fraction of accretion flow may go to the outflow. Probably the powerful outflow is launched at outer parts of the accretion disk and it is not by chance that we can see this strong correlation of the iron line EW with the radio flux. Thus there are two ways for the matter to proceed: i. in the outflow if the local mass accretion rate in the disk exceeds the critical value (which is proportional to radius, see TSA07), ii. in the disk where the matter proceeds and it ultimately converges onto BH. This final stage of the accretion we observe as a saturation of index with mass accretion flow (converging flow signature).

Whereas we do not find any correlation between radio and X-ray fluxes during the spectral transition, although, probably, we see an indication of X-ray-radio connection during a minor flare event. In Figure 16 we show the spectral and timing properties of X-ray emission of a typical minor X-ray/radio flare. As one can see from this Figure (see low panels there) the PDS and energy spectra are different at the peak of the flare from those before and after the flare. Specifically the soft component is more pronounced but QPO features are not seen at the peak of the flare while they are present before and after the flare. Moreover the flat part (white noise) of the peak PDS is extended to higher frequencies (break frequency $\nu_b \sim 10$ Hz at the peak vs $\nu_b \sim 2$ Hz before and after the flare).

In §3.3 we reported the results of the study the energy dependence of the PDS shape and integrated power variability as a function of the photon energy. In Figure 16 we show two power spectra for two energy bands 2-15 keV (red) and 15-30 keV (blue). One can see that PDSs weakly depend on the energy band. We can suggest that the sizes of the photon emission areas L_{CC} related to these two energy bands are also the same. In fact, Titarchuk et al. (2001) argue that ν_{QPO} is proportional to the ratio of magneto-acoustic (plasma) velocity V_{MA} and Compton cloud size L_{CC} and hence one can conclude that the emission areas are the same because ν_{QPO} are the same for these two energy bands.

Lightman & Eardley (1974), hereafter LE74, suggest that the thin disk is always unstable in the inner region when radiation pressure dominates gas pressure. Using numerical simulations Lightman (1974) found that the innermost region of a disk around a BH is

secular unstable against clumping of the gas into rings which observational appearances can be seen by the Earth observer as X-ray-radio flares. We can speculate that an increase of the soft and hard components in the observable X-ray spectrum at the flare peak (compare panels B2 and A2, C2 of Fig. 16) can be a sign that the radiation pressure gets to dominate in the inner disk region. On the other hand the sign of the destruction of some part of the innermost part of the disk, as an effect of the high pressure instability, should be seen in the PDS. TSA07 argue that the break frequency ν_b in PDS is proportional to the diffusion frequency $\nu_d = 1/t_{visc} \sim \hat{\nu}/R^2$ where $\hat{\nu}$ is a viscosity, t_{visc} is a viscous timescale and R is a radial size of the innermost part of the disk. Given that ν_b increases at the peak with respect of that before and after the flare (compare panels B1 and A1, C1 of Fig. 16) it can imply that the size R decreases when ν_b increases, i.e. some part of the innermost part of the disk is probably destroyed.

In terms of the diffusion theory, this disk instability arises in the inner region where the viscous stress W is a decreasing function of the surface density Σ and thus an effective diffusion coefficient of the nonlinear equation for Σ becomes *negative* there [see Eqs. 4-5 in LE74]. On the other hand Makeev & Titarchuk (2009, in preparation), hereafter MT09, obtain this disk instability as a solution the linear diffusion equation for Σ and they do not specify any (ad hoc) assumption about the nature of the disk viscosity (cf. LE74). They just assume the power-law viscosity distribution over the disk and they use the TLM98 angular velocity distribution in the transition layer (TL).

MT09 study the TSA07 model of the PDS formation and they find that this model predicts the existence of the two distinct zones within the TL of the black hole or neutron star, with oppositely different types of diffusion of perturbation taking place in each zone. A simple fact of the change of sign of the angular velocity derivative in the linear diffusion equation for Σ at the critical radius R_{max} results in a *negative* diffusion coefficient of the equation in the interval $R_{in} < r < R_{max}$. Moreover the change of sign of the diffusion coefficient at R_{max} leads to a turnover of the angular momentum transfer, changing it towards the central body of the accreting system, instead of being pushed outwards as in the Keplerian disk. One of the considered scenarios implies an unstable diffusion of the perturbations in the TL inner zone which might be an indication of the development of a X-ray flare followed by a radio flare. The absence of any quasiperiodic oscillations in the TL and raising ν_b are possible indications of this instability.

5. Conclusions

We concentrate our efforts on the study of the correlation between the spectral index and the accretion disk luminosity. We argue that the shape of the correlation pattern can contain the direct BH signature. Namely, we show both observationally and theoretically that the index saturates with mass accretion rate which is a signature of a converging flow. This index saturation effect can exist only in BH sources. Also this correlation pattern carries the most direct information on the BH mass and the distance to the source (see ST09).

We compiled the state transition data from GRS 1915+105 collected with the *RXTE* mission. We examined the correlation between the photon index of the Comptonized spectral component, its normalization and the QPO frequency (see Figs. 6-10, 13-14).

The spectral data of GRS 1915+105 are well fitted by two (soft and hard) BMC components for most of analyzed IS and HSS spectra (see Fig. 3) while LHS spectra essentially require only one BMC component. In addition to two BMC components 8 IS-HSS spectra require an extra component which can be fitted by “high temperature BB-like” profile. We suggest this “BB” component is probably a signature of the redshifted annihilation line formed in the very narrow shell near a BH horizon due to high photon compactness taking place during intermediate and high-soft states (see Fig. 4 and Table 7).

A remarkable result of our study is that the index - normalization (mass accretion rate) correlation seen in GRS 1915+105 is predicted by the theory of the converging flow. We demonstrate that a strong index saturation vs disk flux seen in the index-disk flux correlation (see Fig. 13) is an observational signature of the presence of the converging flow, which should only exist the BH sources. In other words, *this index saturation effect provides a robust observational evidence for the presence of black hole in GRS 1915+105.*

We also find a tight positive correlation of QPO frequencies with the index (see Fig. 14) and consequently that with the disk flux.

Our comprehensive analysis of X-ray and radio emissions in GRS 1915+105 shows that QPOs are seen independently of radio activity of the source during the spectral transition from low-hard to high-soft state. Specifically these QPO features have been detected at any level of the radio flux and even when the radio emission is at the noise level (see left and right panels in Fig. 15 correspondingly). We also do not find any correlation between X-ray and radio fluxes and X-ray power-law index. (see Fig. 11). However, we establish a strong correlation between equivalent width of iron line and radio flux in binary GRS 1915+105 (see Fig. 12).

We are grateful to the referee whose constructive suggestions help us to improve the

paper quality. We acknowledge productive discussion with Nikolai Shaposhnikov and Ada Paizis and we also would like to thank Guy Pooley who kindly provided us *Ryle Radio Telescope* data.

A. The light aberration effect

For a given electron velocity \mathbf{v} moving inward along radius $\mathbf{v} = -v\mathbf{e}_r$ the directions of the ray in the observed laboratory and comoving electron frames \mathbf{n}_0 and \mathbf{n} are related to aberration formula [see e.g. Rybicki & Lightman (1979)]

$$\cos \theta = \frac{v/c - \cos \theta_0}{(v/c) \cos \theta_0 - 1}. \quad (\text{A1})$$

where $\gamma = [1 - (v/c)^2]^{-1/2}$ is Lorentz factor, $\cos \theta_0 = -(\mathbf{n}_0 \cdot \mathbf{e}_r)$ and $\cos \theta = -(\mathbf{n} \cdot \mathbf{e}_r)$ are for the laboratory (zero) and electron rest frames respectively.

For $\gamma \gg 1$, we can write that $1 - v/c = 1/(2\gamma^2)$ and thus we can rewrite Eq. (A1) as follows

$$\cos \theta \sim \frac{-2 \sin^2(\theta_0/2) + 1/(2\gamma^2)}{2 \sin^2(\theta_0/2) + \cos \theta_0/(2\gamma^2)}. \quad (\text{A2})$$

If $\theta_0 \sim b/\gamma$ then for $b > 1$

$$\cos \theta \sim \frac{1 - b^2}{1 + b^2} < 0 \quad (\text{A3})$$

i.e. ray is directed against the electron direction. In fact, $\cos \theta \sim -1$ for *all* $\theta_0 \gg 1/\gamma$. On the other hand

$$\cos \theta = -(\mathbf{n} \cdot \mathbf{e}_r) > 0 \quad (\text{A4})$$

if $b < 1$.

REFERENCES

- Basko, M. M., Sunyaev & Titarchuk, L. G. 1974, *A&A*, 31, 249
- Belloni, T., Klein-Wolt, M., Méndez., M., van der Klis, M., & Paradijs, J. 2000, *A&A*, 355, 271
- Belloni, T., Homan, J., Casella, P., van der Klis, M., Nespoli E., et al. 2005, *A&A*, 440, 207
- Bradshaw, C. F., Titarchuk, L. & Kuznetsov, S.I. 2007, *ApJ*, 663, 1225

- Chakrabarti, S.K. & Titarchuk, L. 1995, *ApJ*, 455, 623 (CT95)
- Coppi, P.K. 1999 in *High Energy Processes in Accreting Black Holes*, ed. J. Poutanen, & R. Svensson, *ASP Conf. Ser.*, 161, 375
- Corbel, S. & Fender, R. P. 2002, *ApJ*, 573, L35
- Giannios, D. 2005, *A&A*, 437, 1007, Paper III
- Grove J.E. et al. 1998, *ApJ*, 500, 899
- Fender, R.P. & Belloni, T. 2004, *ARA&A*, 42, 317 (FB04)
- Fender, R.P. 2001, *MNRAS*, 322, 31
- Klein-Wolt, M., & van der Klis, M. 2008, *ApJ*, 675, 1407
- Kotani, T., Ebisawa, K., Dotani, T. et al. 2000, *ApJ*, 539, 413
- Kylafis, N. D., Papadakis, I. E., Reig, P., Giannios, D. & Pooley, G. G. 2008, *A&A*, 489, 481
- Laming, J.M. & Titarchuk, L. 2004, *ApJ*, 615, L121
- Laor, A. 1991, *ApJ*, 376, 90
- Laurent, P. & Titarchuk, L. 1999, *ApJ*, 511, 289 (LT99)
- Laurent, P. & Titarchuk, L. 2009, in preparation
- Laurent, P. & Titarchuk, L. 2007, *ApJ*, 656, 1056 (LT07)
- Lightman, A. P. 1974, *ApJ*, 194, 429
- Lightman, A. P. & Eardley, D. M. 1974, *ApJ*, 187, L1
- Magdziarz, P., & Zdziarski, A.A. 1995, *MNRAS*, 273, 837 (MZ95)
- Markoff, S., Falcke, H., Fender, R. 2001, *A&A*, 372, L25
- Markoff, S., Nowak, M., Corbel, S., Fender, R. & Falcke, H. 2003, *A&A*, 397, 645
- Martocchia, A., Matt, G., Karas, V., Belloni, T., & Feroci, M. 2002, *A&A*, 387, 215
- McClintock, J. & Remillard, R. 2006, in *Compact Stellar X-ray Sources*, eds. W. H. G. Lewin & M. van der Klis (Cambridge: Cambridge Univ. Press), p. 157
- Meyer-Homeister, E. & Meyer, F. 2003, *A&A*, 402, 1013

- Meyer, F., Liu, B. & Meyer-Homeister, E. 2000, *A&A*, 361, 175
- Meyer-Homeister, E. & Meyer, F. 1999, *A&A*, 348, 154
- Migliari, S., Fender, R.P. & van der Klis, M. 2005, *MNRAS*, 363, 112
- Miller, J.M. & Homan, J. 2005, *ApJ*, 618, 107
- Montanari, E., Titarchuk, L. & Frontera, F. 2009, *ApJ*, 692, 1597
- Muno, M.P., Morgan, E.H. & Remillard, R.A. 1999, *ApJ*, 527, 321
- Neilsen, J. & Lee, J. C. 2009, *Nature*, 458, 481
- Pooley G., & Fender R., 1997, *MNRAS* 292, 925
- Reig P., Belloni, T. van der Klis, M. & Mendez M. 2000, *ApJ*, 541, 883
- Remillard, R. A., & McClintock, J. E. 2006, *ARA&A*, 44, 49
- Rodriguez J., Hannikainen D.C., Shaw S.E. et al. 2008, *ApJ*, 676, 1436
- Różańska, A. & Madej, J. 2008, *MNRAS*, 386, 1872
- Rybicki, G. B., & Lightman, A. P. 1979, *Radiative processes in astrophysics*, New York, Wiley-Interscience (RL79)
- Shaposhnikov, N., Titarchuk, L. & Laurent, P. 2009, *ApJ*, 699, 1223
- Shaposhnikov, N., & Titarchuk, L. 2009, *ApJ*, (ST09)
- Shaposhnikov, N., & Titarchuk, L. 2007, *ApJ*, 663, 445 (ST07)
- Shaposhnikov, N., & Titarchuk, L. 2006, *ApJ*, 643, 1098 (ST06)
- Sunyaev, R.A. & Titarchuk, L.G. 1980, *A&A*, 86, 121
- Swank, J.H. 1999, *Nucl. Phys. B - Proc. Suppl.*, 69, 12, 569, 362
- Titarchuk, L., Bradshaw, C. F. & Wood, K.S. 2001, *ApJ*, 560, L55
- Titarchuk, L.G. & Fiorito, R. 2004, *ApJ*, 612, 988 (TF04)
- Titarchuk, L., Lapidus, I.I. & Muslimov, A. 1998, *ApJ*, 499, 315 (TLM98)
- Titarchuk, L. 2002, meeting abstract, 4th COSPAR Scientific Assembly, The Second World Space Congress, held on October 10-19, 2002 in Houston, TX, USA

- Titarchuk, L., Mastichiadis, A., & Kylafis, N. D., 1997, *ApJ*, 487, 834
- Titarchuk, L., Shaposhnikov, N. & Laurent, P. 2009, *ApJ*, in press, [arcXiv0906.1490](https://arxiv.org/abs/0906.1490) [astro-ph]
- Titarchuk, L. & Shaposhnikov, N. 2008, *ApJ*, 678, 1230
- Titarchuk, L. & Shaposhnikov, N. 2005, *ApJ*, 626, 298
- Titarchuk, L., Shaposhnikov, N. & Arefiev, V. 2007, *ApJ*, 660, 556 (TSA07)
- Titarchuk, L. & Zannias, T. 1998, *ApJ*, 493, 863 (TZ08)
- Trudolyubov, S., Churazov E., Gilfanov M. 1999, *Astronomy Letters*, 25, 718
- Trudolyubov, S. 2001, *ApJ*, 558, 276
- Vadawale, S. V., Rao, A. R. & Chakrabarti, S. K. 2001, *A&A*, 372, 793
- Vignarca, F., Migliari, S., Belloni, T., Psaltis, D., & van der Klis, M. 2003, *A&A*, 397, 729 (V03)

Table 1. Best-fit parameters of spectral analysis of PCA and HEXTE observation of GRS 1915+105 in 3-150 keV energy range during rise 1997 transition[†]. Parameter errors (put in parenthesis) correspond to 1 σ confidence level.

Observational ID	MJD day	$\alpha_1 = \Gamma_1 - 1$	$\log(A_1)^{\dagger\dagger}$	$N_{bmc1},$ L_{39}/d_{10}^2	$\alpha_2 = \Gamma_2 - 1$	$\log(A_2)^{\dagger\dagger}$	$N_{bmc2},$ L_{39}/d_{10}^2	EW, eV	E_{laor} keV	Flux ^{†††}	χ_{red}^2 (d.o.f.)
20402-01-11-00	50462.06	0.867(9)	0.106(4)	0.115(3)	1.84(7)	2.0	0.009(3)	-	-	13.59	1.09 (73)
20402-01-12-00	50471.06	0.844(7)	0.102(3)	0.1105(2)	1.9(2)	2.0	0.009(2)	-	-	13.28	1.06 (73)
20402-01-13-00	50477.87	0.92(2)	0.030(6)	0.116(1)	1.9(3)	2.0	0.002(5)	-	-	13.12	1.01 (73)
20402-01-16-00	50501.88	0.83(1)	0.100(6)	0.1014(5)	2.0(4)	2.0	0.008(2)	-	-	12.01	1.07 (73)
20402-01-19-00	50517.04	0.62(1)	0.137(2)	0.101(1)	1.8(2)	2.0	0.002(1)	-	-	12.16	1.02 (73)
20402-01-20-00	50524.92	0.85(1)	0.077(8)	0.092(2)	1.9(3)	2.0	0.01(2)	-	-	11.51	1.05 (73)
20402-01-21-00	50533.83	0.94(1)	0.050(3)	0.100(1)	2.0(4)	2.0	0.009(5)	-	-	11.34	1.09 (73)
20402-01-21-01	50534.90	0.95(1)	0.025(3)	0.101(1)	2.0(2)	2.0	0.009(2)	-	-	11.30	1.06 (73)
20402-01-23-00	50548.45	0.91(3)	-0.082(8)	0.112(2)	2.0(1)	2.0	0.01(3)	-	-	11.55	1.09 (73)
20402-01-24-00	50561.13	0.72(3)	0.095(4)	0.116(5)	2.0(3)	2.0	0.01(4)	-	-	14.27	1.08 (73)
20402-01-28-00	50586.68	1.59(2)	-0.178(8)	0.2001(2)	2.34(3)	2.0	0.109(1)	-	-	18.59	1.07 (73)
20402-01-29-00	50589.49	0.95(2)	0.033(3)	0.159(1)	2.0(2)	2.0	0.01(3)	-	-	18.00	1.07 (73)
20402-01-30-01	50596.20	1.59(1)	0.32(2)	0.200(8)	2.3(1)	2.0	0.110(2)	-	-	20.45	1.03 (73)
20402-01-31-00	50602.53	1.79(2)	0.07(4)	0.223 (5)	2.6(1)	0.09(6)	0.118(5)	-	-	23.56	1.01 (73)
20402-01-31-02	50604.61	1.80(5)	-0.11(8)	0.218(7)	2.6(1)	0.8(1)	0.127(6)	-	-	23.67	1.08 (73)
20402-01-33-00	50617.54	1.99(6)	0.13(6)	0.22(4)	3.2(2)	0.18(1)	0.24(1)	-	-	30.21	1.01 (73)
20402-01-34-01	50621.80	1.92(4)	0.49(9)	0.22(1)	3.1(1)	-0.18(2)	0.17(1)	-	-	27.18	1.07 (73)
20402-01-35-00	50636.62	1.85(6)	0.030(3)	0.24(4)	3.10(9)	2.0	0.21(5)	-	-	31.54	0.97 (73)
20402-01-36-00	50639.62	1.99(9)	-0.40(1)	0.20(1)	3.2 (1)	2.0	0.256(5)	-	-	32.24	0.97 (73)
20402-01-37-01	50641.48	1.90(9)	-0.26(9)	0.245(9)	3.09(9)	2.0	0.24(1)	-	-	34.38	1.03 (73)
20402-01-38-01	50649.42	1.9(1)	-1.66(8)	0.370(9)	3.20(5)	2.0	0.30(1)	63 (8)	6.1 \pm 0.7	38.59	1.10 (73)
20402-01-39-02	50658.51	2.0(1)	-0.58(7)	0.26(2)	3.2(3)	2.0	0.303(2)	61(10)	6.1 \pm 1.5	38.15	1.12 (73)
20402-01-41-01	50679.30	2.0(1)	-1.82(9)	0.417(6)	3.15(5)	0.7(1)	0.422(8)	78(10)	6.1 \pm 1.0	46.47	1.10 (73)
20402-01-41-02	50679.37	2.00(9)	-1.40(8)	0.459(2)	3.20(1)	2.0	0.429(1)	82(10)	6.09 \pm 0.8	49.90	1.08 (73)
20402-01-43-00	50688.24	2.00(5)	-0.19(6)	0.342(5)	3.20(7)	2.0	0.236(3)	124(14)	6.12 \pm 0.6	41.87	1.01 (73)
20402-01-45-00	50698.65	1.90(1)	-0.22(9)	0.231(2)	3.20(2)	0.47(5)	0.236(2)	151(13)	5.78 \pm 1.4	31.22	0.96 (73)

[†] The spectral model of the continuum is $wabs * (bmc + bmc * highecut + laor)$, ^{††} when parameter $\log(A) > 1.0$, this parameter is fixed to a value 2.0 (see comments in the text), ^{†††}spectral flux in the 3 – 150 energy range in units of $\times 10^{-9}$ ergs/s/cm².

Table 2. Best-fit parameters of spectral analysis of PCA and HEXTE observation of GRS 1915+105 in 3-150 keV energy range during middle 1997 transition. Parameter errors (put in parenthesis) correspond to 1σ confidence level.

Observational ID	MJD day	$\alpha_1 = \Gamma_1 - 1$	$\log(A_1)^\dagger$	$N_{bmc1},$ L_{39}/d_{10}^2	$\alpha_2 = \Gamma_2 - 1$	$\log(A_2)^\dagger$	$N_{bmc2},$ L_{39}/d_{10}^2	EW, eV	E_{laor} keV	Flux ^{††}	χ_{red}^2 (d.o.f.)
20402-01-45-02	50696.21	1.84(1)	0.35(9)	0.33(1)	2.98(2)	0.56(1)	0.379(2)	133(5)	6.31±0.08	39.45	1.05 (73)
20402-01-45-03	50700.25	1.96(4)	-0.1(2)	0.23(4)	3.19(6)	0.49(2)	0.245(8)	192(8)	6.10±0.08	33.49	1.01 (73)
20402-01-46-00	50703.41	2.00(7)	0.02(1)	0.25(2)	3.1(2)	0.8(4)	0.13(2)	87(10)	6.25±0.08	26.96	1.09 (73)
20402-01-48-00	50720.59	2.00(7)	0.77(4)	0.240(6)	3.09(3)	0.15(2)	0.24(1)	164(13)	6.46±0.05	39.44	1.08 (73)
20402-01-50-00	50735.54	1.74(7)	0.16(5)	0.222(8)	3.2(2)	2.0	0.323(9)	125(19)	6.48±0.01	20.69	1.02 (73)
20402-01-50-01	50737.40	1.720(2)	2.0	0.236(1)	1.9(4)	2.0	0.02(2)	102(16)	6.47±0.04	19.19	1.02 (73)
20402-01-51-00	50743.29	1.704(2)	1.9(6)	0.226(1)	2.0(3)	2.0	0.04(5)	102(13)	6.47±0.03	20.56	1.09 (73)
20402-01-52-01	50751.68	2.00(4)	0.15(9)	0.240(6)	3.2(1)	2.0	0.271(6)	348(19)	6.31±0.01	34.60	1.02 (73)
20402-01-52-02	50751.75	2.00(8)	0.06(1)	0.320(2)	3.2(1)	2.0	0.482(5)	342(20)	6.44±0.01	49.68	1.04 (73)
20402-01-53-00	50752.01	2.00(2)	-0.46(1)	0.32(1)	3.00(7)	2.0	0.43(1)	315(10)	6.10±0.01	48.71	0.99 (73)
20402-01-53-02	50756.41	2.00(2)	-0.45(3)	0.39(1)	3.20(1)	2.0	0.32(2)	53(12)	6.18±0.07	43.76	1.01 (73)
20402-01-54-00	50763.20	1.99(8)	2.0	0.412(6)	3.20(3)	2.0	0.369(7)	58(16)	6.19±0.08	45.09	1.02 (73)
20402-01-55-00	50769.22	0.8(3)	0.08(6)	0.01(6)	3.15(3)	0.322(1)	0.426(4)	101(13)	6.25±0.09	35.88	1.02 (73)

[†] When parameter $\log(A) > 1.0$, this parameter is fixed to a value 2.0 (see comments in the text), ^{††}spectral flux in the 3 – 150 energy range in units of $\times 10^{-9}$ ergs/s/cm².

Table 3. Best-fit parameters of spectral analysis of PCA and HEXTE observation of GRS 1915+105 in 3-150 keV energy range during decay 1997 transition. Parameter errors (put in parenthesis) correspond to 1σ confidence level.

Observational ID	MJD day	$\alpha_1 =$ $\Gamma_1 - 1$	$\log(A_1)^\dagger$	$N_{bmc1},$ L_{39}/d_{10}^2	$\alpha_2 =$ $\Gamma_2 - 1$	$\log(A_2)^\dagger$	$N_{bmc2},$ L_{39}/d_{10}^2	EW, eV	E_{laor} keV	Flux ††	χ_{red}^2 (d.o.f.)
30184-01-01-00	50908.00	1.81(2)	0.32(2)	0.260(1)	2.0(3)	2.0	0.009(1)	284(18)	5.75 \pm 1.2	24.90	1.09 (73)
30703-01-14-00	50909.87	1.74(1)	0.55(2)	0.236(1)	2.0(5)	2.0	0.007(2)	317(20)	6.39 \pm 0.05	22.85	1.30 (73)
30402-01-09-00*	50912.88	1.50(2)	-0.32(9)	0.20(3)	2.09(5)	2.0	0.11(1)	290(18)	5.7 \pm 0.3	23.89	1.04 (71)
30402-01-10-00	50914.39	1.50(1)	-0.32(8)	0.1949(8)	2.09(2)	2.0	0.111(9)	411(30)	5.7 \pm 0.4	22.92	1.02 (73)
30402-01-11-00	50923.26	2.00(3)	1.0(2)	0.24(1)	3.2(1)	2.0	0.23(3)	308(20)	5.6 \pm 0.2	31.28	1.23 (73)
30703-01-15-00	50925.88	1.79(5)	0.37(6)	0.22(3)	2.1(1)	2.0	0.10(1)	316(10)	6.4 \pm 0.2	23.79	1.01 (73)
30703-01-16-00	50931.67	1.79(4)	0.37(6)	0.21(3)	2.10(9)	2.0	0.09(2)	326(8)	6.4 \pm 0.3	23.52	1.07 (73)
30402-01-12-01	50945.01	1.69(2)	0.42(3)	0.206(4)	2.10(8)	-0.5(1)	0.094(2)	290(10)	5.7 \pm 0.5	22.17	1.06 (73)
30182-01-02-00	51003.21	1.801(2)	2.0	0.223(2)	2.0(3)	2.0	0.009(1)	434(11)	6.41 \pm 0.01	26.11	0.99 (73)
30182-01-04-01	51006.21	1.0(4)	-1.953(8)	0.169(8)	2.49(6)	2.0	0.125(2)	-	-	24.23	1.03 (73)
30402-01-17-00	51067.62	1.520(3)	0.6(1)	0.200(1)	2.1(3)	2.0	0.009(2)	-	-	21.15	0.98 (73)
30703-01-33-00	51071.90	1.141(7)	0.19(1)	0.172(1)	2.0(4)	2.0	0.002(3)	-	-	19.52	1.07 (73)
30703-01-35-00	51081.81	0.88(3)	0.18(4)	0.152(2)	2.1(2)	2.0	0.009(1)	-	-	18.18	1.02 (73)

† When parameter $\log(A) > 1.0$, this parameter is fixed to a value 2.0 (see comments in the text), †† spectral flux in the 3 – 150 energy range in units of $\times 10^{-9}$ ergs/s/cm 2 , *the data are fitted with $wabs*(bmc+bmc*highcut+laor+tbody)$ model, see values of the best-fit BB color temperature and EW in Table 7.

Table 4. Best-fit parameters of spectral analysis of PCA and HEXTE observation of GRS 1915+105 in 3-150 keV energy range during rise 2005 transition. Parameter errors (put in parenthesis) correspond to 1σ confidence level.

Observational ID	MJD day	$\alpha_1 = \Gamma_1 - 1$	$\log(A_1)^\dagger$	N_{bmc1} , L_{39}/d_{10}^2	$\alpha_2 = \Gamma_2 - 1$	$\log(A_2)^\dagger$	N_{bmc2} , L_{39}/d_{10}^2	EW, eV	E_{laor} keV	Flux ‡†	χ_{red}^2 (d.o.f.)
80701-01-48-00	53382.39	1.78(5)	-0.96(1)	0.125(1)	2.1(4)	2.0	0.009(2)	-	-	6.25	1.05 (73)
90701-01-46-00	53400.35	2.00(1)	-0.21(2)	0.292(4)	2.90(1)	1.1(4)	0.335(1)	91(10)	6.35±0.01	29.94	0.96 (73)
80701-01-37-00	53416.34	2.00(4)	2.0	0.164(1)	2.92(3)	2.0	0.157(4)	594(10)	5.5±0.2	24.03	1.03 (73)
90701-01-49-00	53422.30	2.00(1)	0.26(9)	0.152(4)	3.00(2)	0.75(5)	0.158(4)	626(15)	6.56±0.02	22.30	1.01 (73)
90105-05-03-00	53442.98	1.9(1)	2.0	0.204 (3)	2.92(4)	2.0	0.1574(6)	435(15)	6.45±0.01	24.37	1.06 (73)
90105-05-03-04	53444.01	1.981(6)	2.0	0.191(3)	2.7(0.1)	0.880(2)	0.111(2)	402(12)	6.45±0.01	23.08	1.09 (73)
90105-05-03-05*	53444.08	1.982(4)	2.0	0.187(1)	2.79(6)	0.88(5)	0.112(1)	378(10)	6.46±0.01	22.67	0.96 (71)
91701-01-04-00*	53456.28	1.981(5)	2.0	0.185(2)	2.79(9)	0.884(1)	0.110(1)	256(15)	6.33±0.01	22.69	0.97 (71)
90105-07-01-00	53472.92	1.980(6)	2.0	0.144(1)	2.85(6)	0.251(1)	0.112(1)	55.6(10)	6.57±0.01	22.07	0.99 (73)
90105-07-02-00	53473.05	1.981(5)	1.0(2)	0.147(5)	2.80(6)	0.272(3)	0.133(3)	75.3(6)	6.55±0.07	22.36	0.99 (73)
90105-07-03-00	53473.97	1.98(1)	2.0	0.147(2)	2.80(8)	2.0	0.135(8)	210(8)	6.39±0.01	22.61	0.96 (73)
91701-01-08-00	53486.12	1.96(6)	2.0	0.16 (3)	3.1(2)	-0.02(3)	0.38(3)	132(11)	6.13±0.04	40.68	1.01 (73)
91102-01-01-00	53488.72	1.60(5)	-0.47(7)	0.123(3)	3.0(1)	-0.0030(5)	0.4705(5)	74(12)	6.32±0.08	38.69	1.08 (73)
91412-01-01-00	53500.32	1.99(2)	-1.10(8)	0.261(1)	3.10(1)	0.235(9)	0.3400(9)	50(16)	6.19±0.09	39.35	1.02 (73)
91701-01-10-00	53501.06	2.0(1)	-1.11(9)	0.338(2)	3.20(2)	0.34(1)	0.456(1)	-	-	51.99	1.11 (73)
91701-01-10-01	53501.12	1.9(1)	-1.06 (8)	0.210(4)	3.20(2)	2.0	0.433(4)	68(9)	6.10±0.04	45.30	1.39 (73)
90105-08-02-00	53503.87	1.90(3)	-0.86 (6)	0.358(1)	3.20(1)	0.802(8)	0.4901(6)	104(10)	6.3±0.1	57.53	1.09 (73)
90105-08-03-00	53504.71	2.00(1)	-0.86(7)	0.242(2)	3.20(1)	0.8(2)	0.278(1)	180(12)	6.11±0.01	37.13	1.02 (73)
91701-01-11-00	53508.06	1.70(3)	-1.7 (9)	0.343(2)	3.10(1)	2.0	0.451(1)	69(10)	6.13±0.04	56.21	1.04 (73)
91701-01-12-00	53515.07	0.8(1)	0.3(1)	0.001 (5)	3.197(7)	2.0	0.3480(1)	90(10)	6.4±0.1	24.18	1.09 (73)
91701-01-13-00	53520.05	0.8(1)	0.9(4)	0.05 (6)	3.200(3)	2.0	0.430(1)	120(10)	6.4±0.1	37.02	1.10 (73)
91701-01-17-00	53547.93	0.7(1)	2.0	0.06 (2)	2.75(3)	-1.106(1)	0.193(1)	95(10)	7.1±0.2	11.24	0.99 (73)
91701-01-19-00	53562.92	0.7(1)	-0.9(5)	0.09 (5)	3.20(1)	0.256(7)	0.4633(7)	100(10)	7.0±0.1	23.69	1.02 (73)
91701-01-20-00	53570.78	0.7(2)	-0.9(3)	0.05 (3)	2.57(1)	-0.537(8)	0.151(1)	125(10)	7.0±0.3	69.91	1.18 (73)
91701-01-24-00	53600.89	0.7(1)	-0.95(5)	0.123 (6)	2.75(9)	-0.627(1)	0.124(1)	100(10)	7.0±0.3	5.90	1.24 (73)
91701-01-25-00	53606.84	0.7(2)	-0.7(3)	0.09 (5)	2.75(7)	-0.626(1)	0.132(1)	100(10)	7.1±0.2	6.22	1.25 (73)
90105-04-01-00	53640.38	0.7(1)	0.4(1)	0.04 (5)	2.16(2)	-0.530(4)	0.1335(4)	127(5)	6.40±0.09	6.64	1.35 (73)

Table 4—Continued

Observational ID	MJD day	$\alpha_1 = \Gamma_1 - 1$	$\log(A_1)^\dagger$	$N_{bmc1},$ L_{39}/d_{10}^2	$\alpha_2 = \Gamma_2 - 1$	$\log(A_2)^\dagger$	$N_{bmc2},$ L_{39}/d_{10}^2	EW, eV	E_{laor} keV	Flux ^{††}	χ_{red}^2 (d.o.f.)
90105-04-03-00	53641.43	1.8(6)	0.70(4)	0.215(4)	3.00(1)	1.1(2)	0.282(3)	114(12)	6.11±0.07	33.96	1.08 (73)
90105-04-03-01	53641.51	1.8(7)	0.48(4)	0.215(4)	3.00(1)	1.1(1)	0.284(3)	108(11)	6.32±0.01	32.26	1.01 (73)

[†] When parameter $\log(A) > 1.0$, this parameter is fixed to a value 2.0 (see comments in the text), ^{††}spectral flux in the 3 – 150 energy range in units of $\times 10^{-9}$ ergs/s/cm², * these data are fitted with *wabs*(bmc*highcut+bmc+laor+tbody)* model, see values of the best-fit parameters in Table 7.

Table 5. Best-fit parameters of spectral analysis of PCA and HEXTE observation of GRS 1915+105 in 3-150 keV energy range during middle 2005 transition. Parameter errors (put in parenthesis) correspond to 1σ confidence level.

Observational ID	MJD day	$\alpha_1 = \Gamma_1 - 1$	$\log(A_1)^\dagger$	$N_{bmc1}, L_{39}/d_{10}^2$	$\alpha_2 = \Gamma_2 - 1$	$\log(A_2)^\dagger$	$N_{bmc2}, L_{39}/d_{10}^2$	EW, eV	E_{laor} keV	Flux ^{††}	χ_{red}^2 (d.o.f.)
91701-01-31-00	53646.76	2.00(2)	2.0	0.17(1)	3.0(1)	2.0	0.176(8)	-	-	22.77	1.03 (73)
91701-01-33-01	53659.98	1.60(1)	2.0	0.087(3)	2.90(6)	2.0	0.143(2)	110(13)	6.35±0.07	25.55	1.03 (73)
91701-01-33-00	53661.70	1.99(1)	2.0	0.112(2)	2.78(1)	2.0	0.403(1)	92(8)	6.30±0.01	36.88	0.99 (73)
91701-01-34-00	53669.69	1.42(1)	2.0	0.055(1)	2.51(1)	2.0	0.189(1)	135(10)	6.32±0.01	21.21	1.08 (73)
91701-01-34-01	53669.75	1.7(2)	-0.57(7)	0.084(2)	1.98(4)	2.0	0.185(1)	-	-	21.14	1.04 (73)
91701-01-35-00	53674.59	1.50(5)	-0.55(2)	0.116(2)	3.00(2)	2.0	0.3127(6)	-	-	23.31	1.01 (73)
90105-06-03-01	53694.90	1.70(3)	-1.4(2)	0.345(1)	3.200(1)	2.0	0.552(1)	-	-	62.96	1.02 (73)
90105-06-03-00	53695.03	1.89(2)	-0.56(7)	0.261(4)	3.20(1)	2.0	0.417(5)	-	-	49.38	1.01 (73)
90105-06-03-02	53695.30	1.7(1)	-0.70(8)	0.282(6)	3.18(3)	2.0	0.389(5)	-	-	48.40	1.07 (73)
91701-01-38-00	53696.56	1.80(8)	-1.1(1)	0.35(1)	3.12(2)	0.235(1)	0.479(1)	-	-	51.76	0.99 (73)
91701-01-38-01	53696.63	2.07(3)	0.68(8)	0.685(4)	2.7(2)	2.0	0.290(3)	-	-	57.06	0.98 (73)
91701-01-39-00	53703.57	1.70(2)	-0.22(9)	0.159(3)	2.90(1)	2.0	0.273(4)	-	-	31.30	1.11 (73)
91701-01-39-01	53703.63	1.734(7)	0.35(2)	0.170(1)	2.98(3)	0.471(1)	0.163(1)	-	-	27.10	1.05 (73)
92092-01-01-01	53704.94	1.74(3)	0.05(1)	0.195(3)	2.9(1)	2.0	0.256(2)	-	-	28.45	1.05 (73)
92092-02-01-01	53706.00	1.91(2)	2.0	0.116(3)	2.9(1)	-0.363(1)	0.229(1)	-	-	22.75	0.95 (73)
92092-03-01-01	53707.68	1.7(3)	-1.6(1)	0.36(2)	3.00(6)	0.470(1)	0.49(1)	-	-	56.72	1.08 (73)
91701-01-39-01	53711.55	1.8(1)	-0.33(5)	0.23(2)	2.9(1)	2.0	0.26(2)	-	-	34.48	0.96 (73)
91701-01-41-01	53718.56	1.77(2)	0.85(3)	0.184(1)	2.1(5)	2.0	0.009(1)	-	-	19.95	1.06 (73)
91701-01-42-00	53723.47	1.701(5)	0.8(1)	0.111(2)	2.90(6)	2.0	0.110(1)	-	-	20.57	1.13 (73)
91701-01-42-01*	53723.54	1.91(1)	2.0	0.129(3)	2.70(6)	2.0	0.1644(5)	-	-	20.57	1.05 (71)
91701-01-43-00*	53730.41	1.91(4)	2.0	0.15(2)	2.7(2)	2.0	0.14(9)	-	-	20.29	0.91 (71)

[†] When parameter $\log(A) > 1.0$, this parameter is fixed to a value 2.0 (see comments in the text), ^{††}spectral flux in the 3 – 150 energy range in units of $\times 10^{-9}$ ergs/s/cm², * these data are fitted with *wabs*(bmc*highcut+bmc+laor+bbody)* model, see values of the best-fit parameters in Table 7.

Table 6. Best-fit parameters of spectral analysis of PCA and HEXTE observation of GRS 1915+105 in 3-150 keV energy range during decay 2005 – 2006 transition. Parameter errors (put in parenthesis) correspond to 1σ confidence level.

Observational ID	MJD day	$\alpha_1 = \Gamma_1 - 1$	$\log(A_1)^\dagger$	$N_{bmc1},$ L_{39}/d_{10}^2	$\alpha_2 = \Gamma_2 - 1$	$\log(A_2)^\dagger$	$N_{bmc2},$ L_{39}/d_{10}^2	EW, eV	E_{laor} keV	Flux ††	χ_{red}^2 (d.o.f.)
91701-01-46-00*	53753.43	1.70(1)	0.6(1)	0.284(7)	3.00(2)	2.0	0.3807(8)	108(10)	5.15±0.06	38.60	0.93 (71)
91701-01-49-00*	53771.51	1.69(1)	2.0	0.221(8)	2.41(3)	2.0	0.0978(2)	-	-	16.00	1.06 (71)
91701-01-50-00*	53778.30	1.65(1)	2.0	0.143(2)	2.54(7)	0.38(1)	0.1055(5)	-	-	17.48	0.95 (71)
91701-01-22-00	53794.31	1.68(2)	2.0	0.143(2)	2.00(7)	-0.79(1)	0.081(2)	-	-	18.60	0.96 (73)
92702-01-01-00	53803.28	1.40(2)	2.0	0.12(1)	1.8(2)	0.29 (1)	0.083(4)	-	-	19.35	1.02 (73)
92702-01-01-01	53803.35	1.50(3)	2.0	0.11(1)	1.8(1)	2.0	0.081(7)	-	-	19.11	1.04 (73)
92702-01-02-01	53809.30	1.353(9)	2.0	0.085(2)	1.74(5)	2.0	0.0798(4)	-	-	16.64	1.22 (73)
92702-01-03-00	53815.19	1.49(2)	2.0	0.094(4)	1.21(6)	-0.20(1)	0.063(2)	-	-	17.46	1.02 (73)
92702-01-05-00	53829.20	0.75(3)	0.14(1)	0.125(1)	1.9(5)	2.0	0.005(3)	-	-	16.98	1.02 (73)
92082-01-05-00	53834.84	1.03(1)	0.13(1)	0.140(2)	2.0(6)	2.0	0.009(2)	-	-	16.05	0.98 (73)
92702-01-07-00	53844.16	1.10(2)	-0.15(2)	0.163(1)	1.9(4)	2.0	0.005(3)	-	-	14.92	1.06 (73)
92702-01-08-00	53851.10	0.94(3)	0.06(1)	0.127(2)	2.0(3)	2.0	0.01(2)	-	-	14.50	1.07 (73)
92702-01-08-01	53851.17	1.13(1)	0.09(1)	0.132(1)	2.0(4)	2.0	0.008(3)	-	-	14.74	0.99 (73)
92702-01-08-02	53851.23	1.04(4)	0.05(2)	0.128(1)	1.9(3)	2.0	0.01(3)	-	-	14.03	0.95 (73)
90105-02-04-00	53852.15	1.09(2)	0.15(1)	0.125(1)	1.8(6)	2.0	0.009(2)	-	-	14.28	0.98 (73)

† When parameter $\log(A) > 1.0$, this parameter is fixed to a value 2.0 (see comments in the text), †† spectral flux in the 3 – 150 energy range in units of $\times 10^{-9}$ ergs/s/cm 2 , * these data are fitted with $wabs*(bmc*highcut+bmc+laor+bbbody)$ model, see values of the best-fit parameters in Table 7.

Table 7. Parameters of the model: $wabs^*(bmc^*highcut+bmc+laor+bbody)$ for selected IS data (see the full list of observations in Tables 1-6). Parameter errors (put in parenthesis) correspond to 1σ confidence level.

Model	Parameter	30402-01-09-00	90105-05-03-05	91701-01-04-00	91701-01-42-01	91701-01-43-00	91701-01-46-00	91701-01-49-00	91701-01-50-00
bmc1									
	$\alpha_1 = \Gamma_1 - 1$	1.50±0.02	1.982±0.004	1.981±0.005	1.91±0.01	1.91±0.04	1.70±0.01	1.69±0.01	1.65±0.01
	kT ₁ (keV)	0.9±0.1	1.1±0.1	1.09±0.1	0.99±0.05	1.00±0.01	1.02±0.02	0.95±0.06	0.89±0.09
	N _{bmc1}	0.20±0.03	0.187±0.001	0.185±0.002	0.129±0.003	0.154±0.015	0.284±0.007	0.221±0.008	0.143±0.002
bmc2									
	$\alpha_2 = \Gamma_2 - 1$	2.09±0.05	2.79±0.06	2.79±0.09	2.70±0.06	2.7±0.2	3.00±0.02	2.41±0.03	2.54±0.07
	kT ₂ (keV)	1.0±0.1	1.0±0.1	1.1±0.1	1.0±0.2	0.99±0.09	1.0±0.2	0.99±0.08	1.1±0.3
	N _{bmc2}	0.11±0.01	0.112±0.001	0.110±0.001	0.1644±0.0005	0.14±0.09	0.3807±0.008	0.0978±0.0002	0.1055±0.0005
laor									
	E _{laor} (keV)	5.7±0.3	6.46±0.01	6.33±0.02	5.39±0.01	5.39±0.01	5.15±0.06	6.40±0.09	6.40±0.02
	N _{laor}	0.073±0.02	0.062±0.001	0.028±0.002	0.06±0.01	0.06±0.01	0.022±0.002	0.016±0.004	0.016±0.003
	EW _{laor} (eV)	290±18	378±10	256±15	150±15	180±10	108±10	100±10	100±10
"bbody"									
	T _{bbody} (keV)	4.1±0.2	4.5±0.3	4.3±0.3	4.4±0.2	4.68±0.09	4.77±0.04	4.47±0.09	4.5±0.1
	N _{bbody}	0.04±0.01	0.011±0.006	0.036±0.006	0.041±0.005	0.009±0.001	0.024±0.006	0.038±0.003	0.048±0.004
	EW _{bbody} (eV)	550±30	430±20	490±40	710±50	390±30	470±30	540±30	630±40
Flux [†]									
		23.89	22.67	22.69	20.57	20.29	38.60	16.00	17.48
	χ^2 (d.o.f.)	1.04 (71)	0.96 (71)	0.97 (71)	1.01 (71)	0.92 (71)	0.93 (71)	1.06 (71)	0.95 (71)
S _{15GHz} ^{††}									
		88±2	156±2	140±2	41±2	51±2	65±2	40±2	20±2

[†]spectral flux in the 3 – 150 energy range in units of $\times 10^{-9}$ erg/s/cm². ^{††}spectral flux density in radio band centered at 15 GHz in units of mJy.

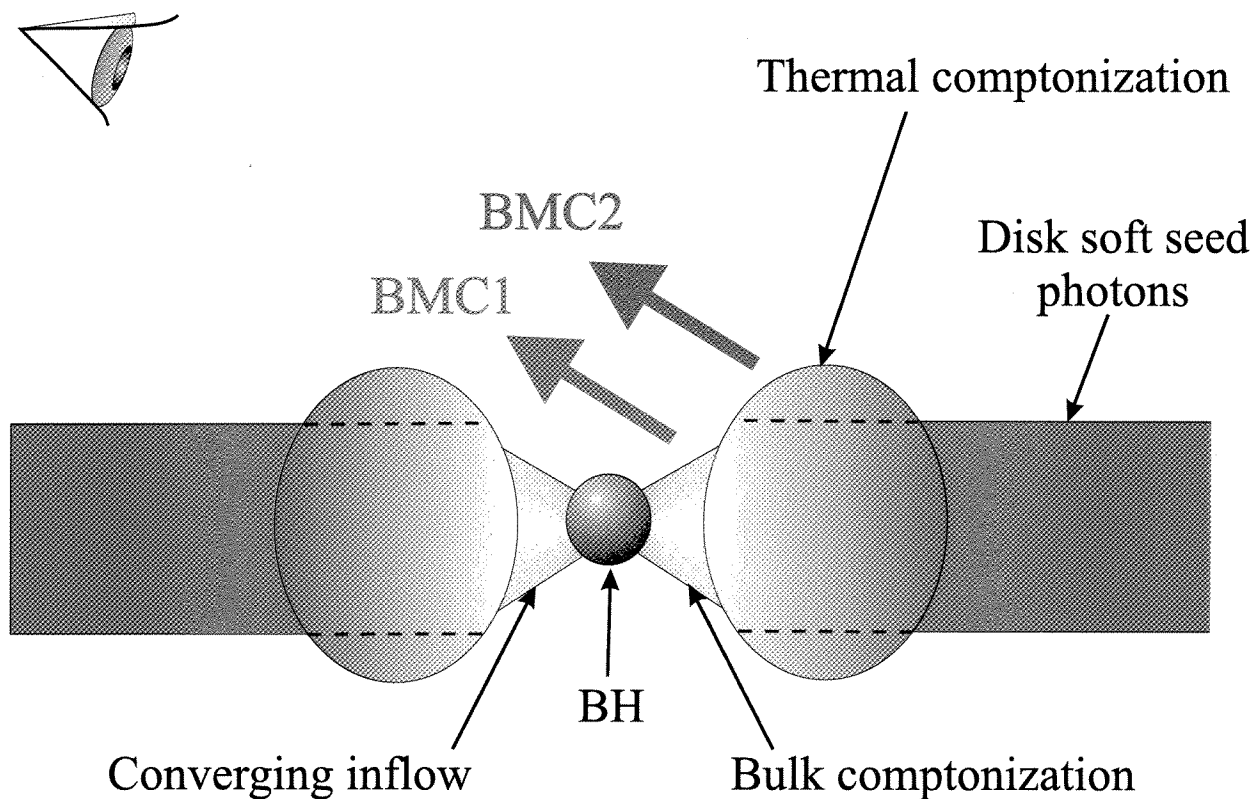


Fig. 1.— Schematic view of the proposed geometry for thermal and bulk Comptonization regions in the source hosting a BH with PL-like emission at high energies. The thermal plus bulk Comptonization spectrum (thermal plus bulk *BMC1*) arises in the innermost part of the transition layer (TL), where the disk BB-like seed photons are (thermally and dynamically) Comptonized by the in-falling material. Whereas the thermal Comptonization spectrum (thermal *BMC2*) originates in the outer part of the TL region.

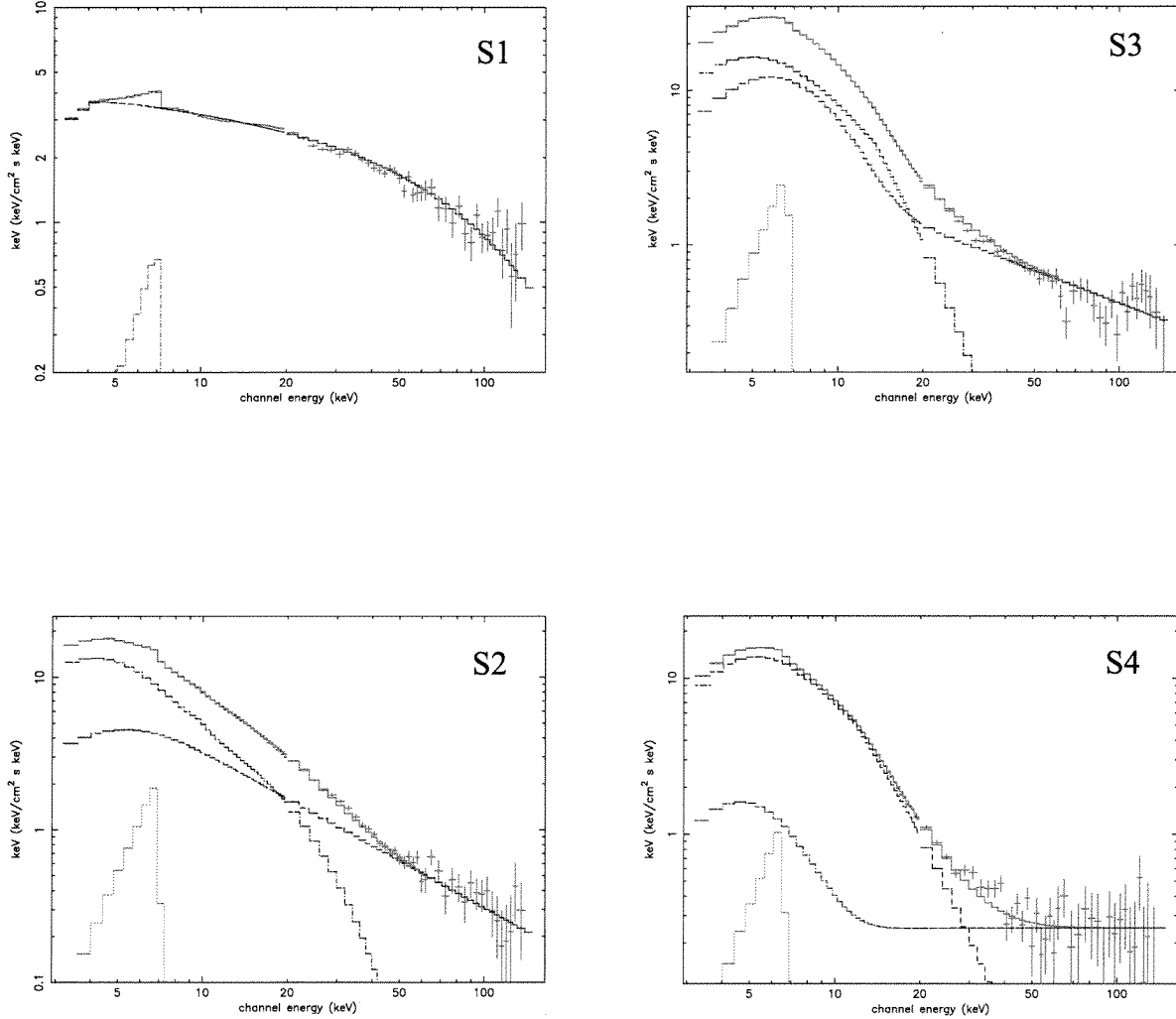


Fig. 2.— Evolution of spectrum shape of GRS 1915+105 during LHS, IS, HSS and VSS spectral states. Data are taken from *RXTE* observations 20402-01-11-00 (*S1*, $\Gamma_1 = 1.8$, LHS), 91701-01-33-00 (*S2*, $\Gamma_1 = 2.9$, $\Gamma_2 = 3.7$, IS), 91701-01-11-00 (*S3*, $\Gamma_1 = 2.7$, $\Gamma_2 = 4.1$, HSS) and 91701-01-19-00 (*S4*, $\Gamma_2 = 4.2$, VSS). Here data are denoted by red points, the spectral model presented with components are shown by blue, black and dashed purple lines for *BMC1*, *BMC2* and *laor* components respectively.

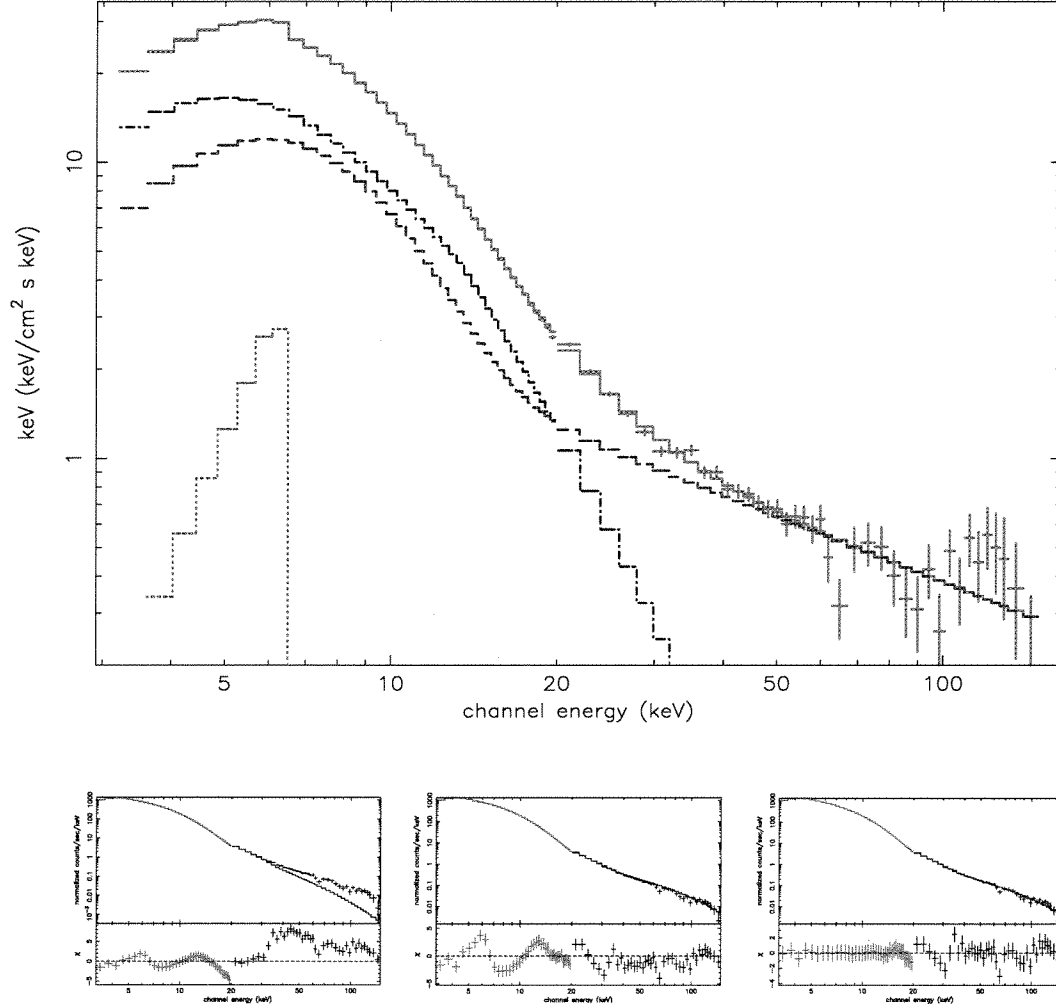


Fig. 3.— The best-fit spectrum of GRS 1915+105 during HSS events of 2005 rise transition (observation 91701-01-11-00) in $E * F(E)$ units (*top*) along with the count spectrum and $\Delta\chi$ (*bottom panels*). *Bottom panels*: *Left*: the best-fit spectrum and $\Delta\chi$ for the model fit, $wabs*bmc*highcut$, which include a single BMC component without an iron line component ($\chi^2_{red}=12.3$ for 75 d.o.f.), *center*: the model fit, $wabs*(bmc+bmc*highcut)$, which includes two BMC components without an iron line component ($\chi^2_{red}=3.28$ for 76 d.o.f.) and *right*: the same as the latter one but adding of the *Laor* line component, $wabs*(bmc+bmc*highcut+laor)$, ($\chi^2_{red}=1.04$ for 73 d.o.f., see Table 4). Blue, black, purple lines stand for *BMC1*, *BMC2* and *Laor* components respectively.

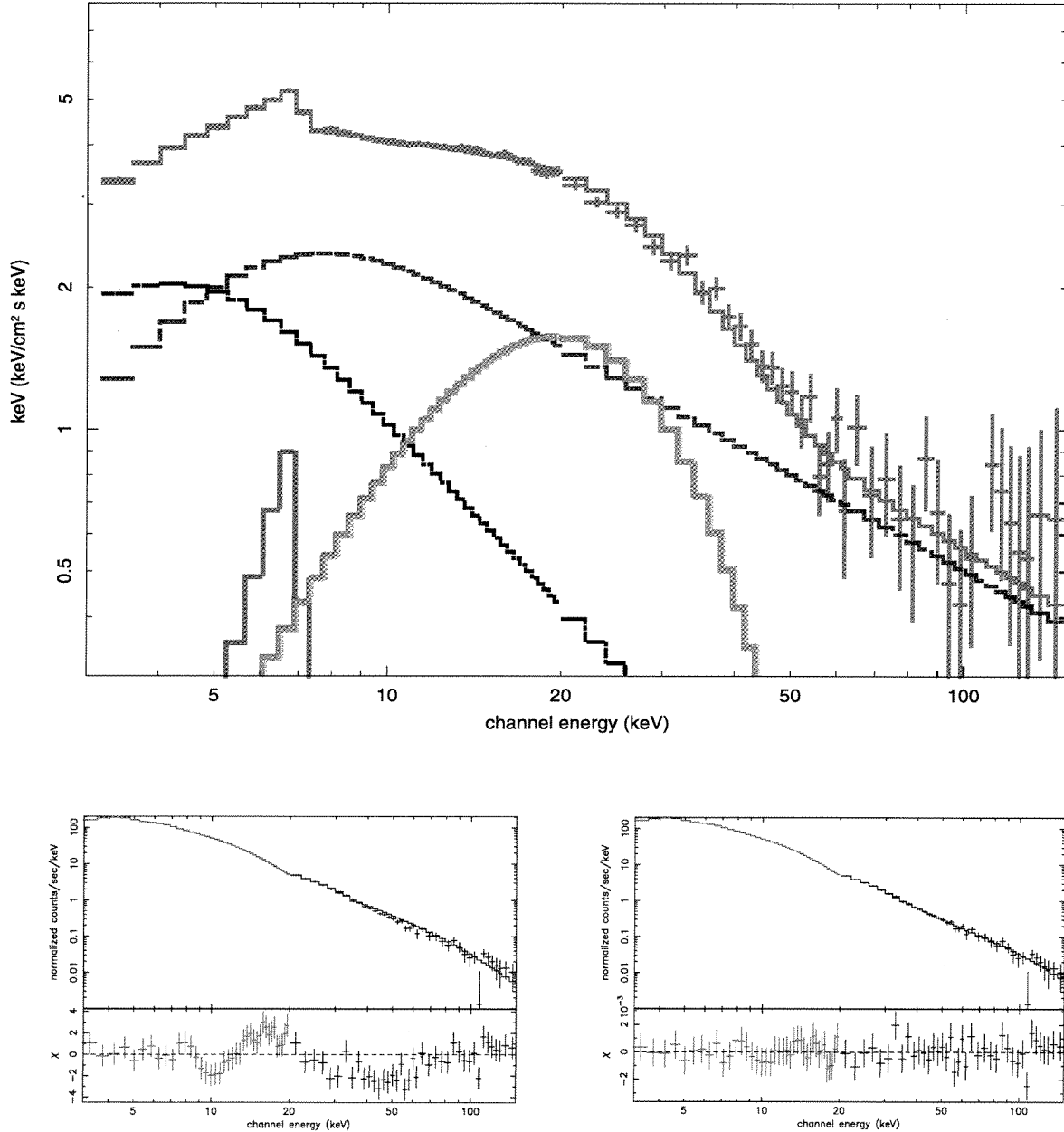


Fig. 4.— The best-fit spectrum during IS-LHS of 2005-2006 decay transition in $EF(E)$ units (*top*) and in normalized counts units (*bottom panel*) with $\Delta\chi$ for the 91701-49-00 observation. *Left*: fitting without modelling the high-temperature “bbody” component ($\chi_{red}^2=1.43$ for 73 d.o.f.) and *right*: the best-fit spectrum and $\Delta\chi$, when the bump in residuals at ~ 20 keV is modelled by a “high-temperature bbody-like” component with $\chi_{red}^2=1.06$ for 70 d.o.f.. On top panel the data are denoted by red points, the spectral model presented with components are shown by blue, black, purple and green lines for *BMC1*, *BMC2*, *laor* and “high-temperature” *bbody* components respectively.

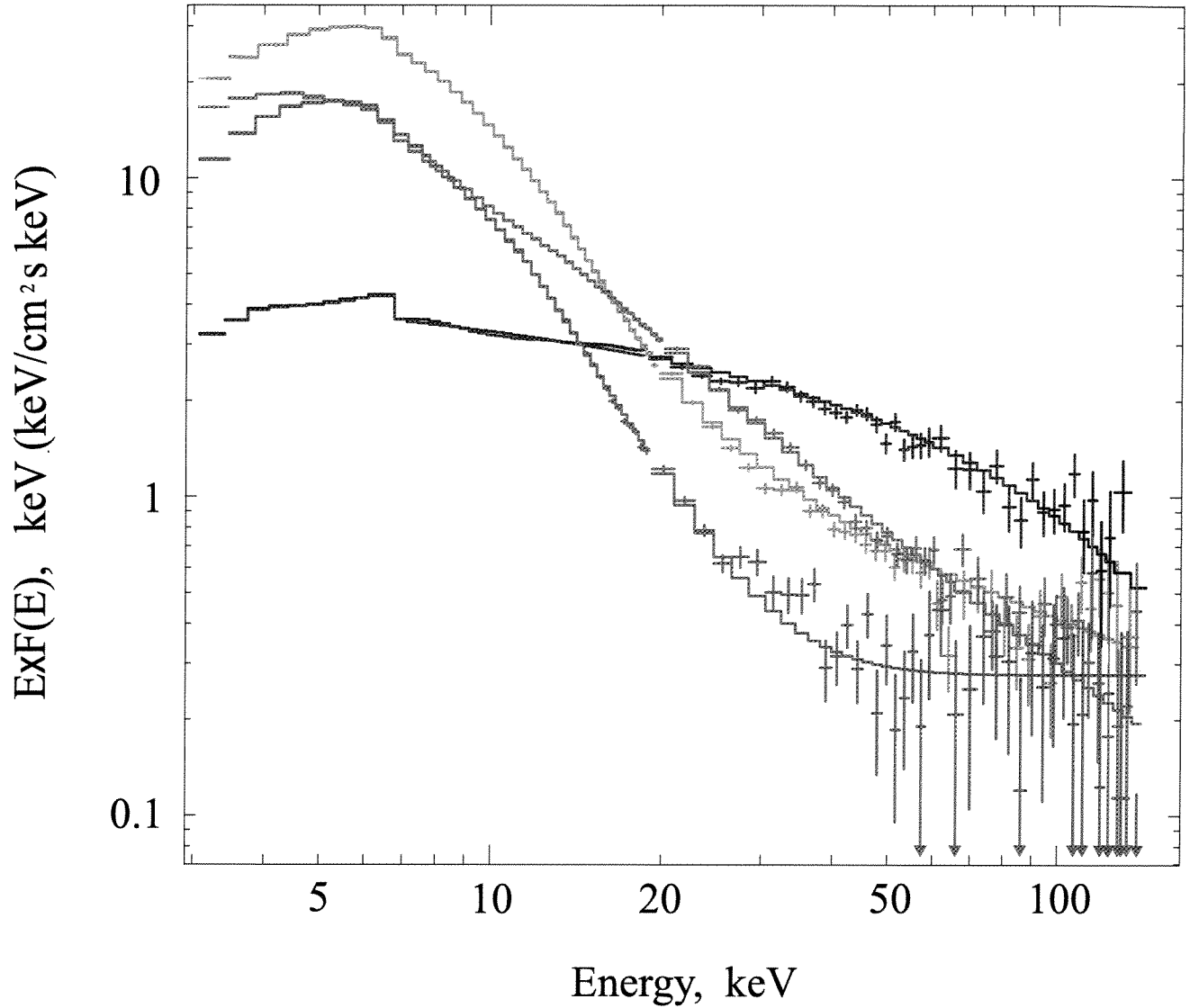


Fig. 5.— Four representative EF_E spectral diagrams during LHS, IS, HSS and VSS spectral states of GRS 1915+105. Data are taken from *RXTE* observations 20402-01-11-00 (*blue*, LHS), 91701-01-33-00 (*red*, IS), 91701-01-11-00 (*green*, HSS) and 91701-01-19-00 (*purple*, VSS).

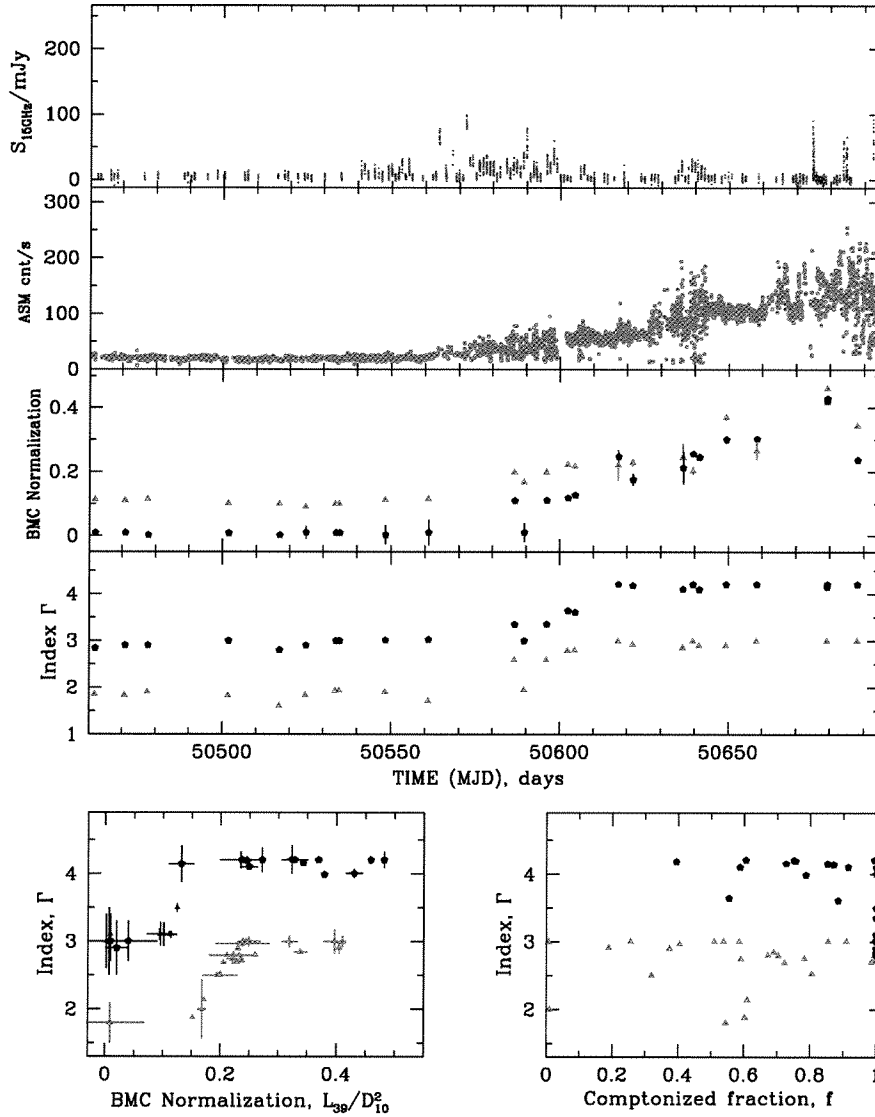


Fig. 6.— *From Top to Bottom:* Evolutions of the flux density S_{15GHz} at 15 GHz (Ryle Telescope), $RXTE/ASM$ count rate, BMC normalization and photon index Γ in the beginning of the 1997 rise transition of GRS 1915+105 (MJD 50460-50700). Red/black points (*for two last panels*) correspond to hard/soft components with Γ_1 and Γ_2 , respectively. *Bottom:* Spectral index Γ plotted versus BMC normalization (*left*) and Comptonized fraction (*right*) for this transition. Here the red triangles/black circles correspond to hard/soft components with Γ_1 and Γ_2 , correspondingly. Note that in most cases the normalization of the hard BMC component ($BMC1$) is higher than that of the soft component ($BMC2$) (see red points vs black points in BMC normalization-time panel).

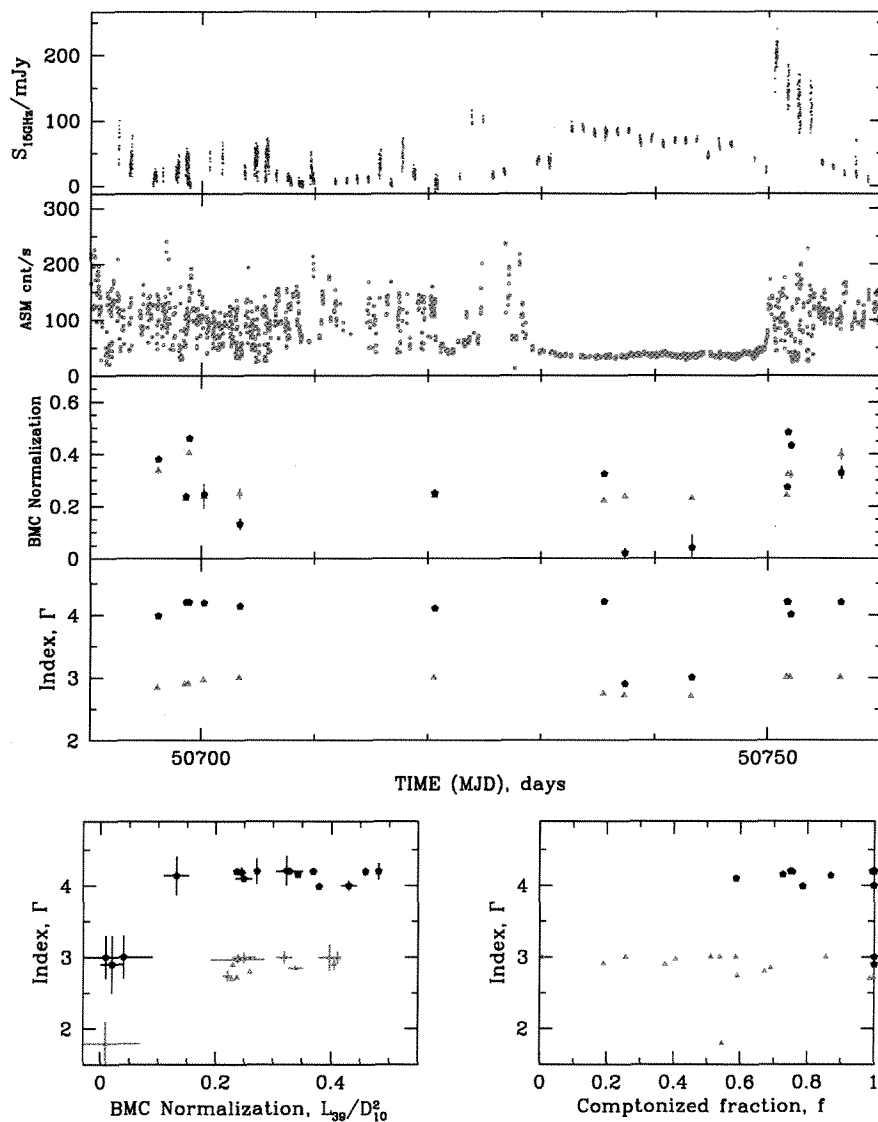


Fig. 7.— *From Top to Bottom:* The same types of evolutions which are presented in Fig. 6 but now that for the middle of the 1997 rise transition of GRS 1915+105 (MJD 50650-50760). In most cases the normalization of the soft BMC component (*BMC2*) is higher than that of the hard component (*BMC1*) [see black points vs red points in BMC normalization - time panel and compare with that in Fig. 6]. The pivoting effect occurs (i.e. $N_{bmc1} > N_{bmc2}$ switches to $N_{bmc2} > N_{bmc1}$ around MJD 50690.

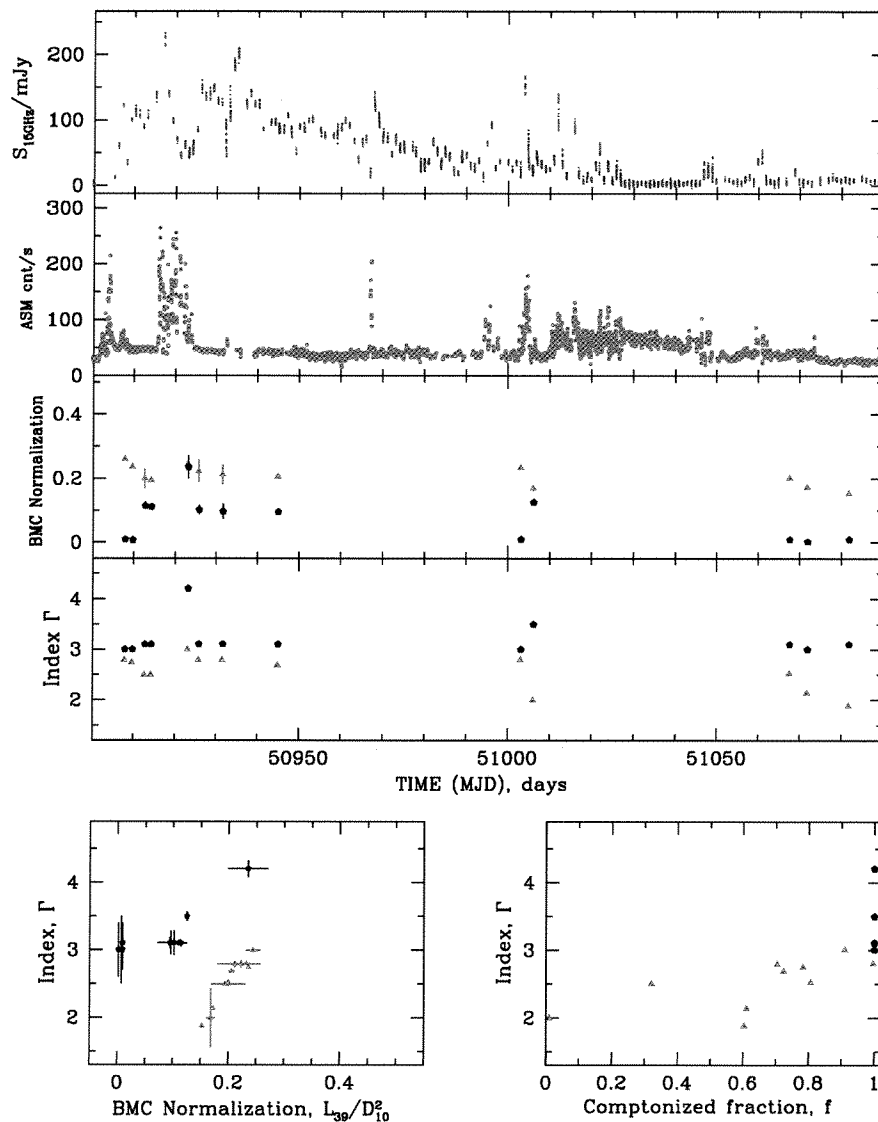


Fig. 8.— *From Top to Bottom:* The same types of evolutions which are presented in Figs. 6–7 but now that for the 1997 – 1998 decay transition of GRS 1915+105. In most cases the normalization of the hard BMC component (*BMC1*) is higher than that of the soft component (*BMC2*) (see red points vs black points in BMC normalization-time panel). The pivoting effect occurs around MJD 50910.

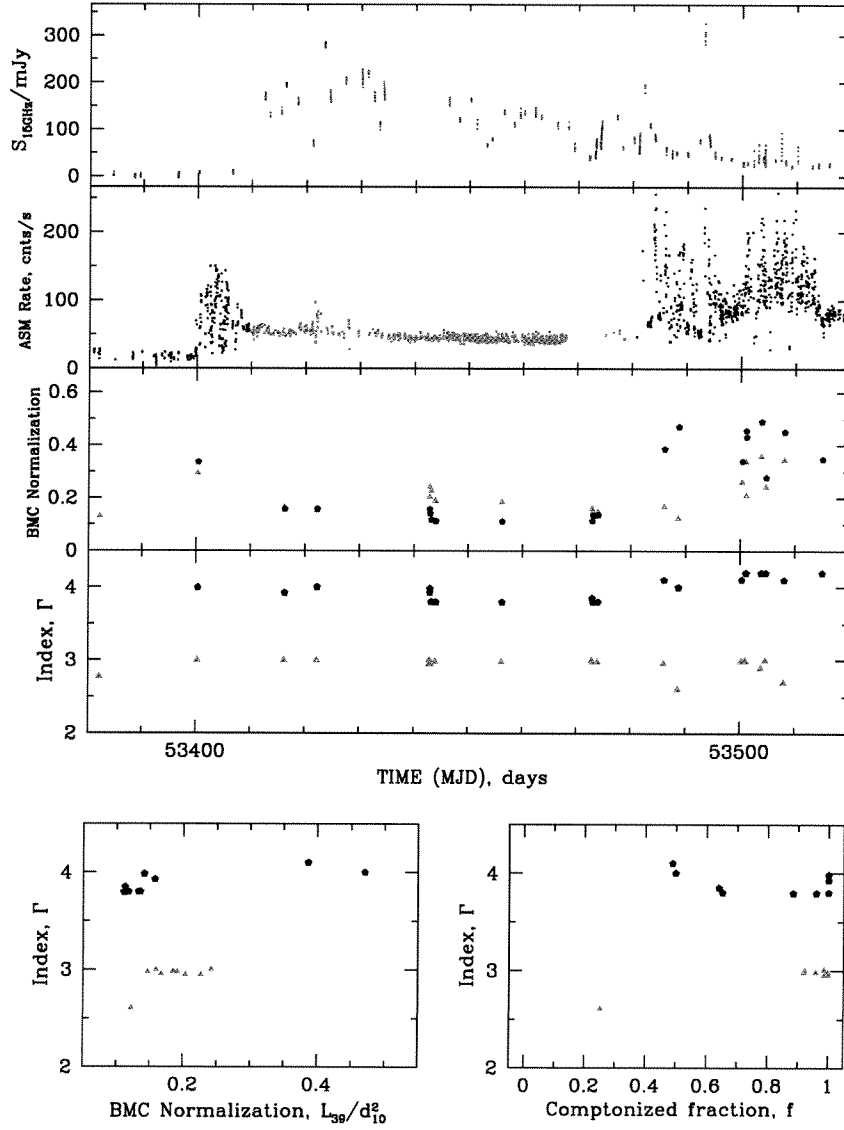


Fig. 9.— *From Top to Bottom:* The same types of evolutions which are presented in Figs. 6-8 but now that for the 2005 rise transition of GRS 1915+105. The pivoting effect occurs around MJD 53475.

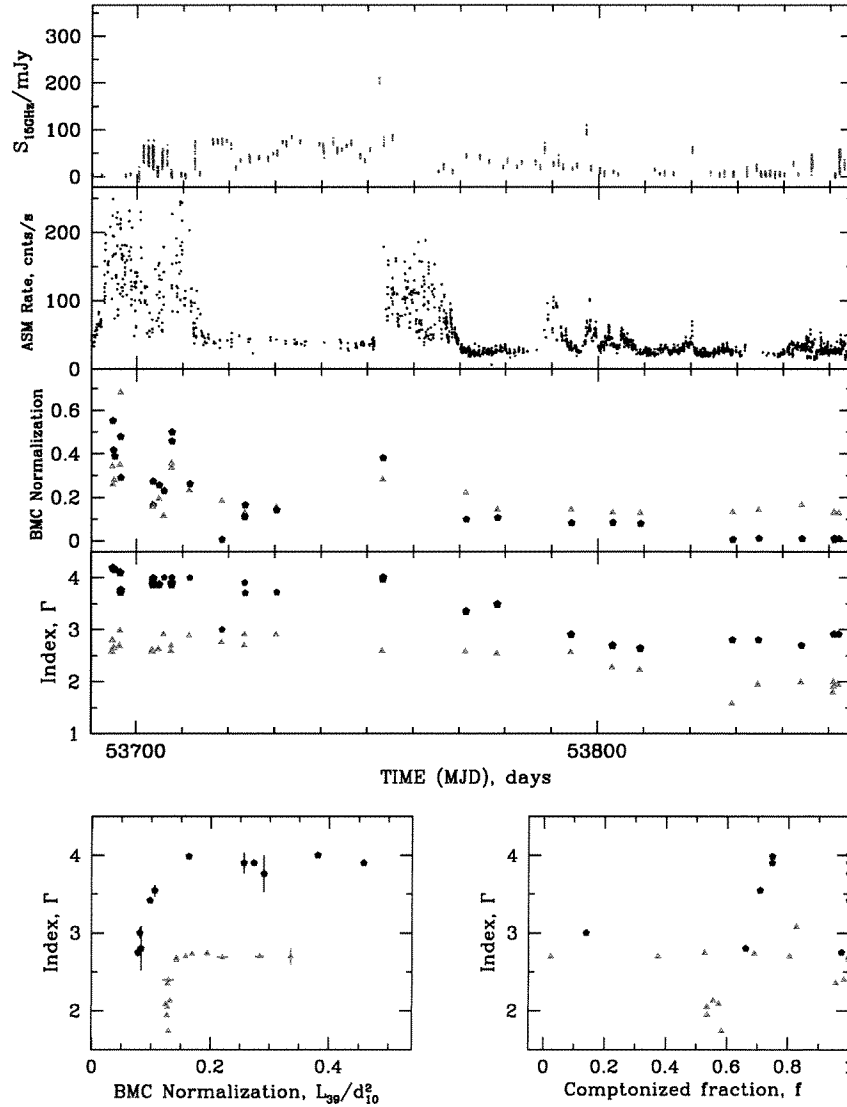


Fig. 10.— *From Top to Bottom:* The same types of evolutions which are presented in Figs. 6-9 but now that for the 2005 – 2006 middle and decay transitions. The pivoting effect occurs between MJD 53750 and MJD 53775.

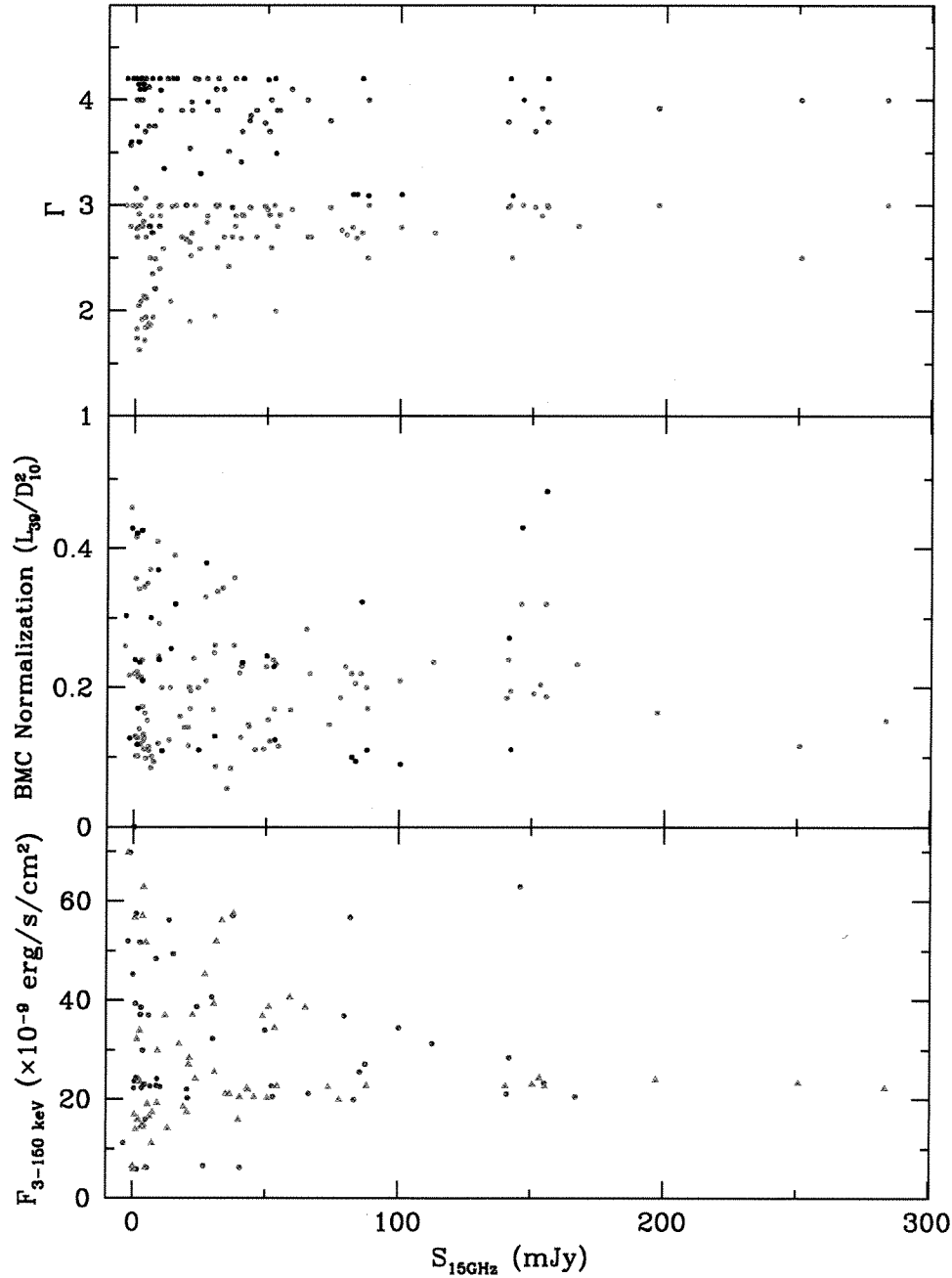


Fig. 11.— BMC photon indices Γ (*top*), normalization (*middle*) and X-ray flux (*bottom*) vs flux density S_{15GHz} . *Top and middle*: Red and black points stand for hard and soft spectral components respectively for the 1997 – 1998 active episode. Crimson and blue points correspond to hard and soft spectral components respectively for the 2005 – 2006 episode. *Bottom*: Blue circles and red triangles stand for 1997 – 1998 and 2005 – 2006.

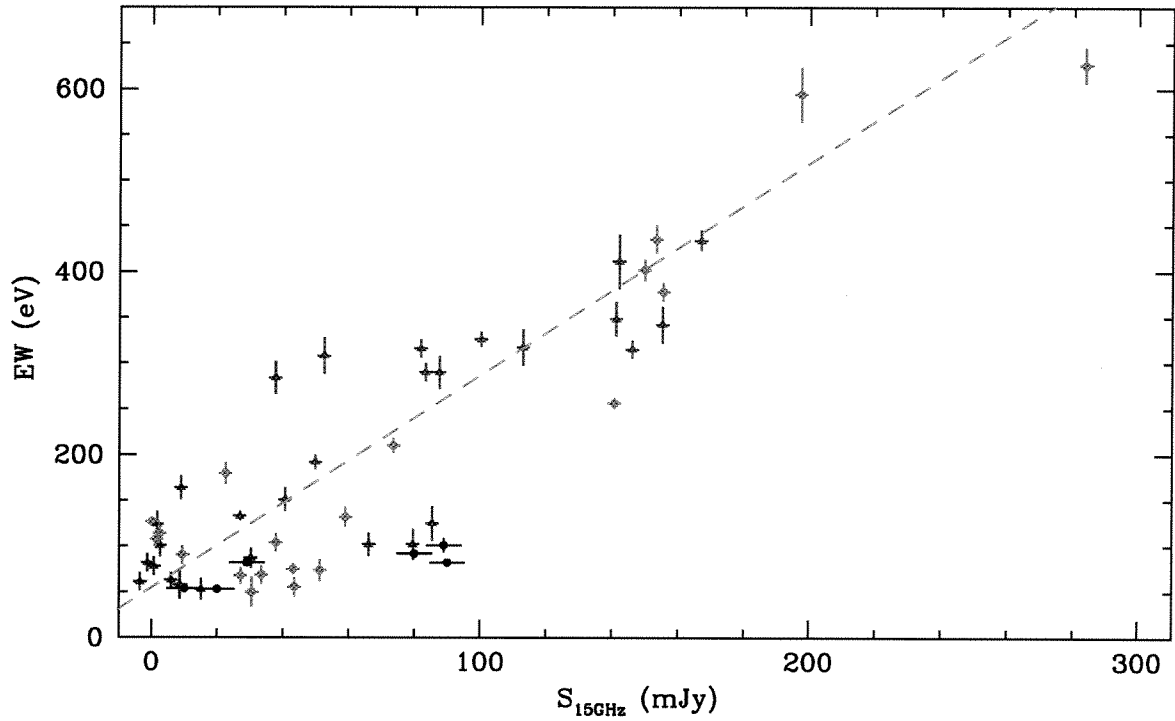


Fig. 12.— The equivalent width (EW) of iron line in eV as a function of flux density $S_{15\text{GHz}}$ at 15 GHz (Ryle Telescope) in mJy for 1997/2005 data sets (blue/red points). Here we also include black points which have been recently found by Neilsen & Lee (2009) analyzing archival HETGS (High Energy Transmission Grating Spectrometer) observations of GRS 1915+105 from the Chandra X-ray Observatory.

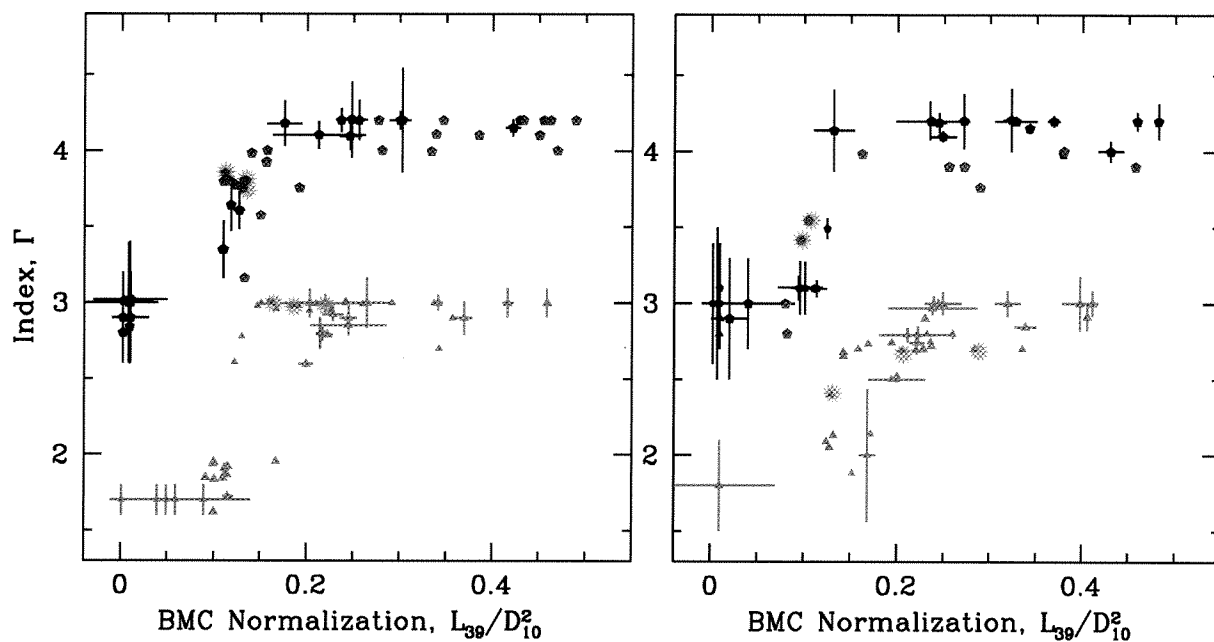


Fig. 13.— Photon index plotted versus BMC normalization for rise (*left*) and decay (*right*) transitions. Red/black points stand for hard/soft spectral components for the 1997 activity episode. Crimson and blue points correspond to hard and soft spectral components respectively for the 2005 episode. Points marked with rose oreol correspond to IS-HSS spectra fitted by the model which includes “high-temperature bbody” component (for details see Fig. 4 and Table 7).

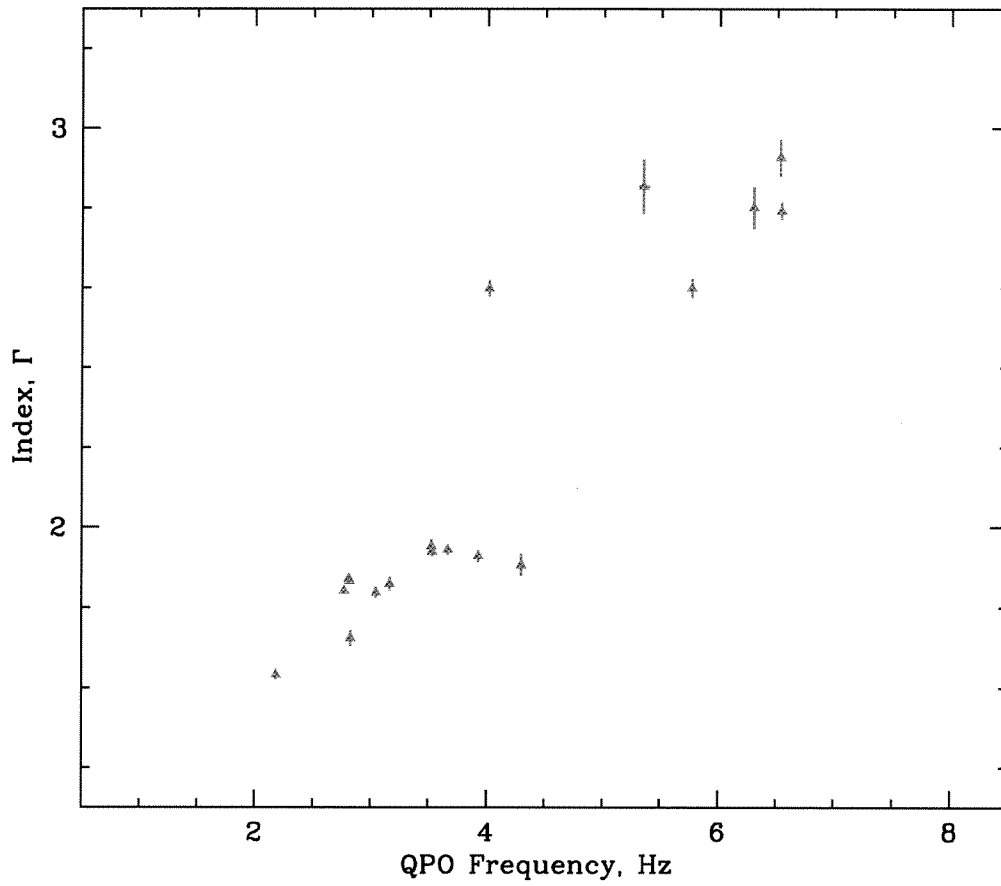


Fig. 14.— Photon index Γ_1 (hard component) plotted versus QPO centroid for the 1997 rise transition from GRS 1915+105.

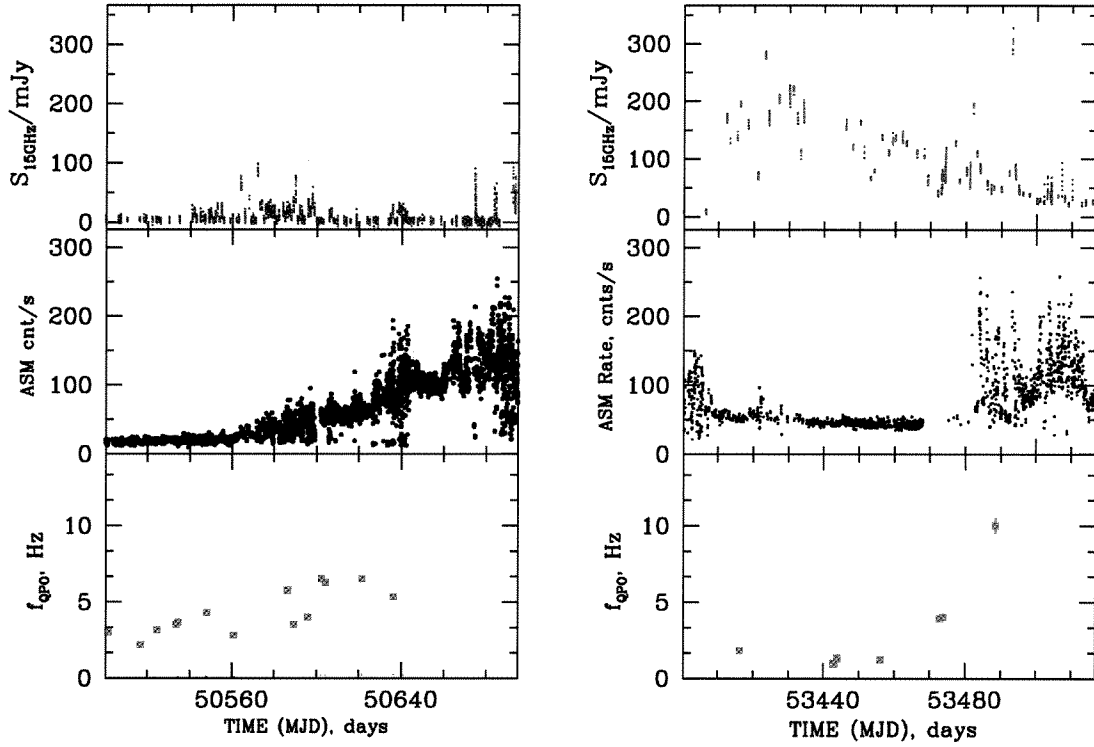


Fig. 15.— Evolution of flux density S_{15GHz} at 15 GHz (Ryle Telescope), *RXTE*/ASM count rate, ν_{QPO} during 1997 (left column) and 2005 (right column) rise transitions of GRS 1915+105. Here ν_{QPO} stands for the centroid frequency of the fundamental QPO. The left column panel demonstrates the presence of QPO even when for radio flux is low (<30 mJy). The right column panel shows an example of the presence of QPOs during prominent radio flux events ($\sim 100 - 200$ mJy). These panels demonstrate that the QPO appearances are independent of the radio flux during LHS-HSS transitions.

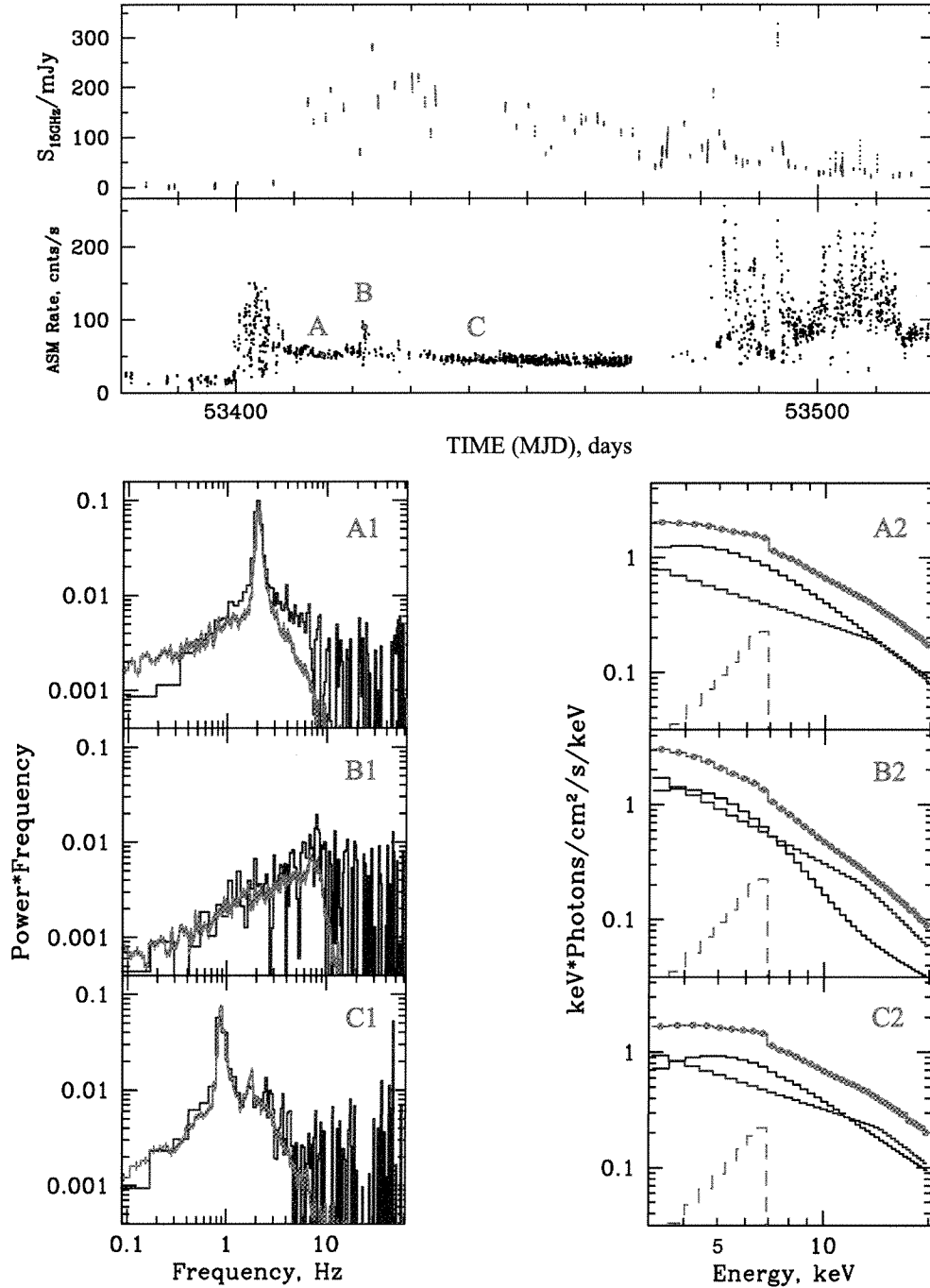


Fig. 16.— *Top*: evolution of the flux density S_{15GHz} at 15 GHz (Ryle Telescope), *RXTE*/ASM count rate during the 2005 rise transition. *Top lower panel*: red points A, B and C mark moments at MJD=53416, 53422 and 53442 (*before, during and after radio flares*) respectively. *Bottom*: PDSs (*left column*) are plotted along with energy spectral diagram $EF(E)$ (*right column*) for three points A (*top*), B (*middle*) and C (*bottom*) of the X-ray light curve. Power density spectra for the soft (red, 3 – 15 keV) and hard (blue, 15 – 30 keV) energy bands are presented. There are QPOs at A and C points (A1, C1 panels) but there is none at B point (B1 panel), at the X-ray flare peak. Here data are denoted by red points, the spectral model presented with components are shown by blue, black and dashed purple lines. The dashed purple line is the total model. The blue and black lines are the soft and hard energy band models respectively.